THE UNIVERSITY OF CHICAGO

HYDRATED PROTON STRUCTURE AND TRANSPORT IN COMPLEX HETEROGENEOUS SYSTEMS

A DISSERTATION SUBMITTED TO

THE FACULTY OF THE DIVISION OF THE PHYSICAL SCIENCES

IN CANDIDACY FOR THE DEGREE OF

DOCTOR OF PHILOSOPHY

DEPARTMENT OF CHEMISTRY

BY

ZHEFU LI

CHICAGO, ILLINOIS

AUGUST 2021

To my parents and Ling

TABLE OF CONTENTS

LIST OF FIGURES

LIST OF TABLES

ACKNOWLEDGEMENTS

First and foremost, I would like to express my greatest gratitude toward my research advisor, Prof. Gregory A. Voth, who has offered me the opportunity to study from him, generously supported my research and provided excellent guidance in science. These past five years of me working with Prof. Voth has been the most rewarding and productive experience in my life. I have been deeply influenced by his insight, passion, dedication and rigorousness towards chemistry.

Also, I would like to extend my gratitude to Prof. Gregory S. Engel and Prof. Laura Gagliardi, for their service on my dissertation committee and precious advice on this thesis.

Additionally, I gratefully acknowledge my distinguished current and past colleagues in the Voth Group, who have created a wonderful academic environment and research experience for everyone. Specifically, I would like to express my appreciation to the following people for collaborating in research, providing advisory or facilitating the operation of our group: Dr. Zhi Wang, Dr. Daniel Beckett, Dr. Yuxing Peng, Dr. Zhi (Shane) Yue, Dr. Xinyou Ma, Dr. Dudu Tong, Dr. Paul Calio, Dr. Chen Chen, Dr. Yining Han, Mr. Chenghan Li, Mr. Won Hee Ryu and Mr. Souvik De.

I am grateful to the kind people from the Church of the Chicagoans, from whom I learned and grew spiritually. And special thanks go to Mr. Han Tang and Mr. Xuliang (Leon) Hou, for being great mentors, helpful friends and faithful brothers.

Finally, I would like to thank my family: my caring partner Ling Ding, my mother Yanhua Wang and my father Wenge Li, for their unconditional support and love these years. I could not have made it this far without them.

ABSTRACT

Hydrated excess proton is ubiquitous in a wide range of systems within the fields of chemistry, biology, materials and engineering. Due to the strength of hydrogen bond (HB) between hydrated excess proton and water molecules, proton transport (PT) in aqueous environments is accompanied by change of molecular topology and breaking/forming of covalent bonds, which give rise to distinct behaviors of excess proton interacting with water. While it has been extensively studied in bulk systems, hydrated excess protons in complex heterogeneous systems remain as an active field of study and have received dedicated research efforts from both experimentalists and theorists.

To capture the reactive nature of PT in aqueous systems, quantum mechanical approaches such as *ab intio* molecular dynamics (AIMD) can be utilized since it does not tether atoms with empirically parametrized covalent bonds. However, since the cost of AIMD simulations is determined by the number of electrons and nuclei in the system, it can be prohibitively expensive to allocate computational resources enough to gain adequate sampling of larger and complicated systems.

Therefore, we employed multiscale reactive molecular dynamics (MS-RMD) methods to understand excess protons in complex aqueous systems, which provides both an accurate description of topology change in PT and manageable computational cost. In MS-RMD, the state of the system is described as a linear combination of "basis states", each of which represents a possible bonding topology of the system. The basis states are then coupled with each other via off-diagonal elements in a Hamiltonian-like matrix and the ground state eigenvector is solved for on

the fly in the MD, which facilitates a realistic description of the PT process at each timestep, as well as an accurate picture of the hydration structure and charge delocalization of the excess proton.

In this thesis, both AIMD and MS-RMD were employed to understand the behaviors of hydrated excess protons in heterogeneous, complex aqueous systems, including: 1) water-vapor interface, 2) reverse-micellar interfaces and 3) protonated water clusters in acetonitrile, in the order from being most bulk-like to least bulk-like. In the system of water-vapor interface, we primarily investigated the interfacial diffusion of excess proton, the surface affinity of the hydrated excess proton with two definitions of the interface: The Gibbs dividing interface (GDI) and the Willard-Chandler interface (WCI). Both the multistate empirical valence bond (MS-EVB) reactive molecular dynamics method and density functional theory-based ab initio molecular dynamics (AIMD) were used to describe the hydrated excess proton specieis, including it "vehicular" (standard diffusion) transport and (Grotthuss) proton hopping transport and associated structures of the hydrated excess proton net positive charge defect. The excess proton is found to exhibit a similar trend and quantitative free energy behavior in terms of its surface affinity as a function of the GDI or WCI. Importantly, the definitions of the two interfaces in terms of the excess proton charge defect are highly correlated and far from independent of one another, thus undermining the argument that one interface is superior to the other when describing the proton interface affinity. Moreover, the hydrated excess proton and its solvation shell significantly influences the location and local curvature of the WCI, making it difficult to disentangle the interfacial thermodynamics of the excess proton from the influence of that species on the instantaneous surface curvature.

Regarding the reverse micelles system, we investigated the solvation and transport properties of hydrated excess protons (with a hydronium-like core structure) in non-ionic Igepal

CO-520 reverse micelles of various sizes in a non-polar solvent. MS-RMD simulations were used to describe vehicular and hopping diffusion during the proton transport process. As detailed herein, an excess proton shows a marked tendency to localize in the interfacial region of micellar water pools. Slow proton transport was observed which becomes faster with increasing micellar size. Further analysis reveals that the slow diffusion of an excess proton is a combined result of slow water diffusion and the low proton hopping rate. This study also confirms that a low proton hopping rate in reverse micelles stems from the interfacial solvation of hydrated excess protons and the immobilization of interfacial water. The low water density in the interfacial region makes it difficult to form a complete hydrogen bond network near the hydrated excess proton, and therefore locks in the orientation of hydrated proton cations. The immobilization of the interfacial water also slows the relaxation of the overall hydrogen bond network.

Finally, we employed molecular dynamics simulations, quantum theory of atoms in molecules (QTAIM) analysis, and free energy sampling to investigate the thermodynamics, structural, and dynamical properties of protonated water clusters solvated in acetonitrile. Multiple species of protonated water clusters were identified in the system, with the primary cluster species being an $H_9O_4^+$ Eigen cation, followed by a three-water $H_7O_3^+$ cation. Further analysis of the structural properties and special pair anisotropy decay trends identifies the $H_7O_3^+$ cluster as an Eigen cation with an acetonitrile replacing one of the solvating water molecules, not a Zundel cation with an additional water molecule as has been previously suggested. The overall Eigen-like nature of the protonated water clusters was found to be the result of the localization of the excessive charge defects. We conclude that an acetonitrile-acid-based water system contains multiple species of Eigen-like protonated water clusters

CHAPTER 1

INTRODUCTION

1.1 Simulation of Proton Transport in Aqueous Systems

Hydrated excess proton is ubiquitous in a wide range of systems within the fields of biology, chemistry, material science, and engineering. Of particular importance are systems involving large molecular species with complex biochemical functionalities such as proteins[1-9] and proton exchange membranes.[10-18] In these systems, the aqueous phase where the excess proton reside and transport are usually heterogeneous and interfacial. Compared to bulk aqueous systems, we are yet to acquire adequate understandings of hydrated excess protons in these heterogeneous, complex systems.

The simplest description of hydrated excess proton is a hydronium (H_3O^+), where the excess proton binds with a water molecule, forming a cation with one excess charge. However, in the setting of aqueous systems, the solvation motif of the excess proton is more complicated. In general, the hydrated excess proton features two limiting solvation motifs: (1) a Zundel cation ($H_5O_2^+$) in which the excess proton simultaneously forms strong hydrogen bonds with two competing water molecules, and (2) an Eigen cation ($H_9O_4^+$) in which the excess proton is closely bound to a central water molecule and solvated by three additional water molecules that form the first solvation shell. The extensive experimental and theoretical studies in literature notwithstanding, the most stable solvation structures and the exact nature of the conversion between the two solvation motifs remain poorly understood.[19-20]

Despite its significance, it can be experimentally challenging to establish atomistic level details of hydrated excess protons and proton transport (PT) due to the currently limited methodologies to characterize chemical processes at single-atom and femtosecond[21-23] level. Therefore, computational and theoretical study of PT has proved its significance, by providing simulation data at a higher spatial and temporal resolution in supplement to experimental data.[24-38] However, modeling hydrated excess protons and PT can post certain challenges due to their complex nature.

Compared to the diffusion of non-reactive particles, the proton transport (PT) process is a combination of at two mechanisms: the vehicular transport of the hydronium cation and the Grotthuss shuttling.[39] During Grotthuss shuttling the hydrogen bonds rearrange, while the covalent bonds of water molecules and hydronium cations break and reform. Accordingly, an accurate physical model of the PT process must capture any topological changes in chemical bonding in order to accurately reflect the essential physics associated with this process. Since in classical MD methods the bonding topology remains static, such approaches fall short in elucidating the detailed behavior of hydrated excess protons in water and related aqueous environments. To capture the reactive nature of PT in aqueous systems, quantum mechanical approaches such as *ab intio* molecular dynamics (AIMD) can be utilized since it does not tether atoms with empirically parametrized covalent bonds. [40-41] However, since the cost of AIMD simulations is determined by the number of electrons and nuclei in the system, it can be prohibitively expensive to allocate computational resources enough to gain adequate sampling of larger and more complicated systems.

Therefore, we employed multiscale reactive molecular dynamics (MS-RMD) [42-44] methods (as well as its predecessor multi-state empirical valance bond methods, MS-EVB) to understand

excess protons in complex aqueous systems, which provides an accurate description of topology change in PT at a manageable computational cost. In MS-RMD, the state of the system is described as a linear combination of "basis states", $|i\rangle$, each of which represents a possible bonding topology of the system. The basis states are then coupled with each other via off-diagonal elements in a Hamiltonian-like matrix and the ground state eigenvector is solved for on the fly in the MD, which facilitates a realistic description of the PT process at any given timestep, as well as the hydration structure of the excess proton. At each time step, the ground state eigenvector of the Hamiltonian gives the populations of each basis state, which are then used to calculate the atomistic forces by applying the Hellman-Feynman theorem. Several MS-EVB models have been developed that are able to accurately describe the behavior of hydrated proton in various systems such as the air-water interface and proton exchange membranes,[45-46] as well as biomolecular systems.[47] Detailed descriptions of the MS-RMD method are presented in Section 1.2.

1.2 Multiscale Reactive Molecular Dynamics (MS-RMD)

Standard classical MD methods is inadequate for capturing the physics of hydrated excess protons and PT processes, due to their incapability of characterizing charge delocalization and change of bonding topology. On the other hand, while AIMD can account for these complex natures of excess protons, the computational cost of performing AIMD can be prohibitively expensive when investigating systems of a larger scale. To overcome these limitations, our group have developed the MS-RMD method to investigate hydrated excess proton in aqueous systems.

In the MS-RMD approach, the delocalized solvation of excess proton is described via a linear combination of a set of basis states $|i\rangle$, each of which represents one possible bonding

topology involving the hydrated excess proton. The state function of the system can be written down as:

$$|\Psi\rangle = \sum_{i}^{N} c_i |i\rangle \tag{1.1}$$

where c_i is the coefficient of each state and N is the total number of states. The state function $|\Psi\rangle$ is obtained by constructing a Hamiltonian matrix:

$$\boldsymbol{H} = \sum_{ij} |i\rangle h_{ij} \langle j| \tag{1.2}$$

where h_{ii} of a diagonal element is the potential energy surface of the diabatic basis state $|i\rangle$ described mostly by a classical force field, and h_{ij} of an off-diagonal element describes the coupling between two basis states, which require further parametrization (see below). The Hamiltonian matrix is diagonalized on-the-fly to solve for the ground-state energy and eigenvectors of the system:

$$\boldsymbol{Hc} = E_0 \boldsymbol{c} \tag{1.3}$$

where E_0 is the ground state energy of the system, and $\boldsymbol{c}$ is the eigenvector. The ground state (or "pivot" state) of the system is defined as the state with the largest coefficient c_i, i.e., the most probable state. The water oxygen atom to which the excess proton is bound in the pivot state is named the "pivot oxygen", which can be used to determine the coordinates of the hydronium cation in the system. On the other hand, the center of excess charge (CEC) of the hydrated excess proton charge defect is used to represent the continuous and time-dependent location of the charge defect created by an excess proton. The CEC is a weighted average of the atomic coordinates of the protons in each basis state, defined as:

$$\boldsymbol{r}_{CEC} = \sum_{i=1}^{N} c_i^2 \, \boldsymbol{r}_{COC}^i \tag{1.4}$$

in which $\boldsymbol{r}_{COC}^i$ is the center of charge of the hydronium cation in the i-th eigenstate, as a function of the instantaneous point in time of an MS-RMD trajectory:

$$\boldsymbol{r}_{COC}^i = \frac{\sum_{k\in\{i\}}|q_k|\boldsymbol{r}_k}{\sum_{k\in\{i\}}|q_k|} \tag{1.5}$$

To propagate the configuration change of the system, the force exerted on each atom can be calculated from Hellmann-Feynman theorem:

$$\boldsymbol{F} = -\sum_{ij} c_i c_j \, \nabla h_{ij} \tag{1.6}$$

The diagonal elements h_{ii} in the Hamiltonian matrix defined by Equation 1.2 are given by the potential energy function of the basis states, as presented in the following expression:

$$h_{ii} = V_{H_3O^+}^{intra} + \sum_{k}^{N_{H_2O}} V_{H_2O}^{intra,k} + \sum_{k}^{N_{H_2O}} V_{H_3O^+,H_2O}^{inter,k} + \sum_{k<k'}^{N_{H_2O}} V_{H_2O}^{inter,kk'} \tag{1.7}$$

where the four potential terms are the intramolecular potential of hydronium cation and water molecules, the intermolecular potential between the hydronium cation and water molecules and among water molecules, respectively. The $V_{H_3O^+}^{intra}$ term is defined as:

$$V_{H_3O^+}^{intra} = \sum_{j}^{3} D_{OH}[1 - e^{-a_{OH}\left(R_{OH}^j - R_{OH}^0\right)}] + \frac{1}{2}\sum_{j}^{3} k_\alpha(\alpha_j - \alpha_0)^2 \tag{1.8}$$

where the R_{OH}^j is the length of the *j*-th of the three O-H bonds in the hydronium cation, α_j is the *j*-th H-O-H angle, and R_{OH}^0 and α_0 are the parameters of bond length and angle from a classical force field. The $\sum_k^{N_{H_2O}} V_{H_3O^+,H_2O}^{inter,k}$ term is defined as:

$$\sum_{k}^{N_{H_2O}} V_{H_3O^+,H_2O}^{inter,k} = 4\epsilon_{OO_w}\left[\left(\frac{\sigma_{OO_w}}{R_{OO_k}}\right)^{12} - \left(\frac{\sigma_{OO_w}}{R_{OO_k}}\right)^{6}\right] + 4\epsilon_{HO_w}\left[\left(\frac{\sigma_{HO_w}}{R_{HO_k}}\right)^{12} - \left(\frac{\sigma_{HO_w}}{R_{HO_k}}\right)^{6}\right] + \sum_{m}^{4}\sum_{n_k}^{3}\frac{q_m^{H_3O^+} q_{n_k}^{H_2O}}{R_{mn_k}} + V_{OO_k}^{rep} + V_{HO_k}^{rep} \tag{1.9}$$

where the first two terms are the Lennard-Jones interactions between hydronium oxygen and water oxygen, and between hydronium hydrogen and water oxygen; the third term denotes the Coulombic interactions; and the last two terms $V_{OO_k}^{rep}$ and $V_{HO_k}^{rep}$ are additional repulsive terms. The last two repulsive terms are found to be necessary to reproduce a correct potential energy surface (PES) between the hydronium cation and water molecules in its first solvation shell. The two terms are defined in the following expressions respectively:

$$V_{HO_k}^{rep} = Ce^{-c\left(R_{HO_k} - d_{OH}^0\right)} \tag{1.10}$$

$$V_{OO_k}^{rep} = Be^{-b\left(R_{OO_k} - d_{OO}^0\right)}\sum_{j}^{3} e^{-b' q_{H_j O_k}^2} \tag{1.11}$$

Other terms of diagonal elements h_{ii} defined in Equation 1.6 are also described in classical MD methods. The off-diagonal elements h_{ij} are given by:

$$h_{ij} = \left(V_{const}^{ij} + V_{ex}^{ij}\right) \cdot A(R_{OO}, \boldsymbol{q}) \tag{1.12}$$

if the state $|i\rangle$ and $|j\rangle$ share a common hydrogen atom and can facilitate a proton transport reaction; Otherwise $h_{ij} = 0$. In Equation 1.11, the V_{const}^{ij} is a parametrized constant and V_{ex}^{ij} represents the electrostatic interaction between a Zundel cation ($H_5O_2^+$) and the remaining $N-1$ water molecules:

$$V_{ex}^{ij} = \sum_{m}^{7} \sum_{k}^{N_{H_2O}-1} \sum_{n_k}^{3} \frac{q_{n_k}^{H_2O} q_m^{ex}}{R_{mn_k}} \tag{1.13}$$

where $q_{n_k}^{H_2O}$ and q_m^{ex} are the exchange charges of the Zundel complex and the atomic charges of the *k*-th water molecule, respectively. The term $A(R_{OO}, \boldsymbol{q})$ is a scaling factor based on geometry:[44]

$$\begin{aligned} A(R_{OO}, \boldsymbol{q}) = e^{-\gamma \boldsymbol{q}^2}\left[1 + Pe^{-k(R_{OO}-D_{OO})^2}\right] \\ \times\left\{\frac{1}{2}\{1 - \tanh\left[\beta(R_{OO} - R_{OO}^0)\right]\} + P'e^{-\alpha(R_{OO}-r_{OO}^0)}\right\} \end{aligned} \tag{1.14}$$

where R_{OO} is the O-O distance in the Zundel complex and $\boldsymbol{q}$ is a spatial vector that denotes the offset between the shared hydrogen atom in the Zundel complex and the center of the two oxygen atoms.

Equations and explanations above describe the full framework of the MS-RMD approach. More detailed rationalizations, table of parameters, processes of parametrization and derivation of functions have been included in extensive discussions in the previous publications of our group (see ref[21, 43-44, 48-54]).

1.3 References

1. Wraight, C. A., Chance and Design—Proton Transfer in Water, Channels and Bioenergetic Proteins. *Biochimica et Biophysica Acta (BBA)-Bioenergetics* **2006**, *1757*, 886-912.

2. Decoursey, T. E., Voltage-Gated Proton Channels and Other Proton Transfer Pathways. *Physiological reviews* **2003**.

3. Cukierman, S., Et Tu, Grotthuss! And Other Unfinished Stories. *Biochimica et Biophysica Acta (BBA)-Bioenergetics* **2006**, *1757*, 876-885.

4. Swanson, J. M.; Maupin, C. M.; Chen, H.; Petersen, M. K.; Xu, J.; Wu, Y.; Voth, G. A., Proton Solvation and Transport in Aqueous and Biomolecular Systems: Insights from Computer Simulations. *The Journal of Physical Chemistry B* **2007**, *111*, 4300-4314.

5. Popović, D. M.; Stuchebrukhov, A. A., Electrostatic Study of the Proton Pumping Mechanism in Bovine Heart Cytochrome <I>C</I> Oxidase. *Journal of the American Chemical Society* **2004**, *126*, 1858-1871.

6. Siegbahn, P. E. M.; Blomberg, M. R. A., Proton Pumping Mechanism in Cytochrome C Oxidase. *Journal of Physical Chemistry A* **2008**, *112*, 12772-12780.

7. Lee, S.; Swanson, J. M. J.; Voth, G. A., Multiscale Simulations Reveal Key Aspects of the Proton Transport Mechanism in the Clc-Ec1 Antiporter. *Biophysical Journal* **2016**, *110*, 1334-1345.

8. Liang, R.; Swanson, J. M. J.; Wikström, M.; Voth, G. A., Understanding the Essential Proton-Pumping Kinetic Gates and Decoupling Mutations in Cytochrome <I>C</I> Oxidase. *Proceedings of the National Academy of Sciences* **2017**, *114*, 5924-5929.

9. Mayes, H. B.; Lee, S.; White, A. D.; Voth, G. A.; Swanson, J. M. J., Multiscale Kinetic Modeling Reveals an Ensemble of Cl-/H+Exchange Pathways in Clc-Ec1 Antiporter. *Journal of the American Chemical Society* **2018**, *140*, 1793-1804.

10. Roy, A.; Hickner, M. A.; Lee, H.-S.; Badami, A.; Yu, X.; Li, Y.; Glass, T.; McGrath, J. E., Transport Properties of Proton Exchange Membranes. *ECS Transactions* **2007**, *2*, 45-54.

11. Petersen, M. K.; Hatt, A. J.; Voth, G. A., Orientational Dynamics of Water in the Nafion Polymer Electrolyte Membrane and Its Relationship to Proton Transport. *The Journal of Physical Chemistry B* **2008**, *112*, 7754-7761.

12. Jorn, R.; Voth, G. A., Mesoscale Simulation of Proton Transport in Proton Exchange Membranes. *Journal of Physical Chemistry C* **2012**, *116*, 10476-10489.

13. Arntsen, C.; Savage, J.; Tse, Y. L. S.; Voth, G. A., Simulation of Proton Transport in Proton Exchange Membranes with Reactive Molecular Dynamics. 2016; Vol. 16, pp 695-703.

14. Savage, J.; Voth, G. A., Proton Solvation and Transport in Realistic Proton Exchange Membrane Morphologies. *Journal of Physical Chemistry C* **2016**, *120*, 3176-3186.

15. Rao, Z.; Zheng, C.; Geng, F., Proton Conduction of Fuel Cell Polymer Membranes: Molecular Dynamics Simulation. *Computational Materials Science* **2018**, *142*, 122-128.

16. Kreuer, K.-D.; Paddison, S. J.; Spohr, E.; Schuster, M., Transport in Proton Conductors for Fuel-Cell Applications: Simulations, Elementary Reactions, and Phenomenology. *Chemical reviews* **2004**, *104*, 4637-4678.

17. Savage, J.; Tse, Y.-L. S.; Voth, G. A., Proton Transport Mechanism of Perfluorosulfonic Acid Membranes. *The Journal of Physical Chemistry C* **2014**, *118*, 17436-17445.

18. Arntsen, C.; Savage, J.; Tse, Y. L.; Voth, G., Simulation of Proton Transport in Proton Exchange Membranes with Reactive Molecular Dynamics. *Fuel Cells* **2016**, *16*, 695-703.

19. Knight, C.; Voth, G. A., The Curious Case of the Hydrated Proton. *Accounts of chemical research* **2012**, *45*, 101-109.

20. Agmon, N.; Bakker, H. J.; Campen, R. K.; Henchman, R. H.; Pohl, P.; Roke, S.; Thämer, M.; Hassanali, A., Protons and Hydroxide Ions in Aqueous Systems. *Chemical reviews* **2016**, *116*, 7642-7672.

21. Schmitt, U. W.; Voth, G. A., The Computer Simulation of Proton Transport in Water. *The Journal of chemical physics* **1999**, *111*, 9361-9381.

22. Markovitch, O.; Chen, H.; Izvekov, S.; Paesani, F.; Voth, G. A.; Agmon, N., Special Pair Dance and Partner Selection: Elementary Steps in Proton Transport in Liquid Water. *The Journal of Physical Chemistry B* **2008**, *112*, 9456-9466.

23. Swanson, J. M.; Simons, J., Role of Charge Transfer in the Structure and Dynamics of the Hydrated Proton. *The Journal of Physical Chemistry B* **2009**, *113*, 5149-5161.

24. Thämer, M.; De Marco, L.; Ramasesha, K.; Mandal, A.; Tokmakoff, A., Ultrafast 2d Ir Spectroscopy of the Excess Proton in Liquid Water. *Science* **2015**, *350*, 78-82.

25. Kundu, A.; Dahms, F.; Fingerhut, B. P.; Nibbering, E. T.; Pines, E.; Elsaesser, T., Hydrated Excess Protons in Acetonitrile/Water Mixtures: Solvation Species and Ultrafast Proton Motions. *The journal of physical chemistry letters* **2019**, *10*, 2287-2294.

26. Dahms, F.; Fingerhut, B. P.; Nibbering, E. T.; Pines, E.; Elsaesser, T., Large-Amplitude Transfer Motion of Hydrated Excess Protons Mapped by Ultrafast 2d Ir Spectroscopy. *Science* **2017**, *357*, 491-495.

27. Fournier, J. A.; Carpenter, W. B.; Lewis, N. H.; Tokmakoff, A., Broadband 2d Ir Spectroscopy Reveals Dominant Asymmetric H 5 O 2+ Proton Hydration Structures in Acid Solutions. *Nature chemistry* **2018**, *10*, 932-937.

28. Carpenter, W. B.; Fournier, J. A.; Lewis, N. H.; Tokmakoff, A., Picosecond Proton Transfer Kinetics in Water Revealed with Ultrafast Ir Spectroscopy. *The Journal of Physical Chemistry B* **2018**, *122*, 2792-2802.

29. Carpenter, W. B.; Lewis, N. H.; Fournier, J. A.; Tokmakoff, A., Entropic Barriers in the Kinetics of Aqueous Proton Transfer. *The Journal of chemical physics* **2019**, *151*, 034501.

30. Petersen, P. B.; Saykally, R. J., Evidence for an Enhanced Hydronium Concentration at the Liquid Water Surface. *Journal of Physical Chemistry B* **2005**, *109*, 7976-7980.

31. Tarbuck, T. L.; Ota, S. T.; Richmond, G. L., Spectroscopic Studies of Solvated Hydrogen and Hydroxide Ions at Aqueous Surfaces. *Journal of the American Chemical Society* **2006**, *128*, 14519-14527.

32. Levering, L. M.; Roxana Sierra-Hernández, M.; Allen, H. C., Observation of Hydronium Ions at the Air-Aqueous Acid Interface: Vibrational Spectroscopic Studies of Aqueous Hcl, Hbr, and Hi. *Journal of Physical Chemistry C* **2007**, *111*, 8814-8826.

33. Tian, C.; Ji, N.; Waychunas, G. A.; Shen, Y. R., Interfacial Structures of Acidic and Basic Aqueous Solutions. *Journal of the American Chemical Society* **2008**, *130*, 13033-13039.

34. Das, S.; Bonn, M.; Backus, E. H. G., The Surface Activity of the Hydrated Proton Is Substantially Higher Than That of the Hydroxide Ion. *Angewandte Chemie International Edition* **2019**, *58*, 15636-15639.

35. Mucha, M.; Frigato, T.; Levering, L. M.; Allen, H. C.; Tobias, D. J.; Dang, L. X.; Jungwirth, P., Unified Molecular Picture of the Surfaces of Aqueous Acid, Base, and Salt Solutions. *Journal of Physical Chemistry B* **2005**, *109*, 7617-7623.

36. Ishiyama, T.; Morita, A., Molecular Dynamics Analysis of Interfacial Structures and Sum Frequency Generation Spectra of Aqueous Hydrogen Halide Solutions. *Journal of Physical Chemistry A* **2007**, *111*, 9277-9285.

37. Das, S.; Imoto, S.; Sun, S.; Nagata, Y.; Backus, E. H.; Bonn, M., Nature of Excess Hydrated Proton at the Water-Air Interface. *Journal of the American Chemical Society* **2019**, *142*, 945-952.

38. Chiang, K.-Y.; Dalstein, L.; Wen, Y.-C., Affinity of Hydrated Proton at Intrinsic Water/Vapor Interface Revealed by Ion-Induced Water Alignment. *Journal of Physical Chemistry Letters* **2020**, *11*, 696-701.

39. Agmon, N., The Grotthuss Mechanism. *Chemical Physics Letters* **1995**, *244*, 456-462.

40. Tuckerman, M.; Laasonen, K.; Sprik, M.; Parrinello, M., Ab Initio Molecular Dynamics Simulation of the Solvation and Transport of H3o+ and Oh-Ions in Water. *The Journal of Physical Chemistry* **1995**, *99*, 5749-5752.

41. Tuckerman, M.; Laasonen, K.; Sprik, M.; Parrinello, M., Ab Initio Molecular Dynamics Simulation of the Solvation and Transport of Hydronium and Hydroxyl Ions in Water. *The Journal of chemical physics* **1995**, *103*, 150-161.

42. Schmitt, U. W.; Voth, G. A., The Computer Simulation of Proton Transport in Water. *Journal of Chemical Physics* **1999**, *111*, 9361-9381.

43. Day, T. J. F.; Soudackov, A. V.; Čuma, M.; Schmitt, U. W.; Voth, G. A., A Second Generation Multistate Empirical Valence Bond Model for Proton Transport in Aqueous Systems. *Journal of Chemical Physics* **2002**, *117*, 5839-5849.

44. Wu, Y.; Chen, H.; Wang, F.; Paesani, F.; Voth, G. A., An Improved Multistate Empirical Valence Bond Model for Aqueous Proton Solvation and Transport. *Journal of Physical Chemistry B* **2008**, *112*, 467-482.

45. Tse, Y. L. S.; Chen, C.; Lindberg, G. E.; Kumar, R.; Voth, G. A., Propensity of Hydrated Excess Protons and Hydroxide Anions for the Air-Water Interface. *Journal of the American Chemical Society* **2015**, *137*, 12610-12616.

46. Arntsen, C.; Savage, J.; Tse, Y. L. S.; Voth, G. A., Simulation of Proton Transport in Proton Exchange Membranes with Reactive Molecular Dynamics. *Fuel Cells* **2016**, *16*, 695-703.

47. Liang, R.; Swanson, J. M. J.; Wikström, M.; Voth, G. A., Understanding the Essential Proton-Pumping Kinetic Gates and Decoupling Mutations in Cytochrome C Oxidase. *Proceedings of the National Academy of Sciences* **2017**, *114*, 5924-5929.

48. Knight, C.; Lindberg, G. E.; Voth, G. A., Multiscale Reactive Molecular Dynamics. *The Journal of chemical physics* **2012**, *137*, 22A525.

49. Yamashita, T.; Peng, Y.; Knight, C.; Voth, G. A., Computationally Efficient Multiconfigurational Reactive Molecular Dynamics. *Journal of chemical theory and computation* **2012**, *8*, 4863-4875.

50. Nelson, J. G.; Peng, Y.; Silverstein, D. W.; Swanson, J. M., Multiscale Reactive Molecular Dynamics for Absolute P K a Predictions and Amino Acid Deprotonation. *Journal of chemical theory and computation* **2014**, *10*, 2729-2737.

51. Maupin, C. M.; Wong, K. F.; Soudackov, A. V.; Kim, S.; Voth, G. A., A Multistate Empirical Valence Bond Description of Protonatable Amino Acids. *The Journal of Physical Chemistry A* **2006**, *110*, 631-639.

52. Biswas, R.; Tse, Y.-L. S.; Tokmakoff, A.; Voth, G. A., Role of Presolvation and Anharmonicity in Aqueous Phase Hydrated Proton Solvation and Transport. *The Journal of Physical Chemistry B* **2016**, *120*, 1793-1804.

53. Izvekov, S.; Parrinello, M.; Burnham, C. J.; Voth, G. A., Effective Force Fields for Condensed Phase Systems from Ab Initio Molecular Dynamics Simulation: A New Method for Force-Matching. *The Journal of chemical physics* **2004**, *120*, 10896-10913.

54. Chen, C.; Arntsen, C.; Voth, G. A., Development of Reactive Force Fields Using Ab Initio Molecular Dynamics Simulation Minimally Biased to Experimental Data. *The Journal of chemical physics* **2017**, *147*, 161719.

CHAPTER 2

WHAT COORDINATE BEST DESCRIBES THE AFFINITY OF THE HYDRATED EXCESS PROTON FRO THE AIR-WATER INTERFACE?

2.1 Introduction

The air-water interface is an important system that has received considerable attention, not only because of its role in various atmospheric and environmental processes, but also due to its significance for ion solvation at dielectric boundary interfaces (for reviews, see, e.g., Refs[1-2]) Despite ongoing research, the behavior of ions near the air-water interface remains somewhat unclear with respect to multiple aspects. A particularly interesting question that continues to spark debate is whether the air-water interface is acidic or basic in comparison to the bulk.

In 2004 Petersen and Voth first predicted the affinity of the hydrated excess proton for the air-water interface, under acidic solution conditions,[3] thus contradicting conventional concepts of cationic solvation that predict cations are buried into the bulk away from the interface. Subsequent experimental efforts involving surface-selective spectroscopies and sum-frequency generation[4-12] have largely supported this prediction, including two very recent and precise experimental studies.[11-12] These reactive molecular dynamics (MD) simulations[3, 13-14] employed the multistate empirical valence bond (MS-EVB) method[15-17] in order to provide a physically accurate

description of the net positive hydrated excess proton charge defect (aka the "hydronium" cation and its association close-by water molecules). These simulations also provided both a qualitative and quantitative molecular level explanation for the unusual surface affinity of the hydrated excess proton. This topic was revisted[18] in 2015 using the newly developed MS-EVB 3.2 model[19] that is capable of more accurately capturing the hydration structure of the excess proton in water as well as it vehicular (standard diffusion) and Grotthuss hopping transport[20] behavior. This 2015 paper also compared the interfacial solvation of the hydroxide anion and found that it does not have an affinity for the interface as compared to the hydrated proton.

A natural question has arisen in these and other studies as to the "best" way to describe the air-water interface, as well as how to define the proximity of the hydrated excess proton to that interface. Conventionally, the Gibbs dividing interface (GDI) is used for identifying the location of the air-water interface in atomistic MD simulations. Specifically, the GDI utilizes the local density of the interfacial species and can be defined as the surface where the local density is half of the bulk density. However, more recently, Willard and Chandler described a procedure[21] for identifying instantaneous liquid interfaces with the density field of molecules under consideration. This so-called Willard-Chandler interface (WCI) is in principle capable of accounting for the fluctuations of an interfacial configuration over time. Accordingly, the WCI can be calculated for every time step during an MD simulation while accounting for the instantaneous shift of the interface due to its fluctuations. Recent work by Wick[22] has also suggested that the surface propensity of the hydrated excess proton can be very different based on the interface used to describe it (i.e., GDI vs WCI). In a related study, but one that could only utilize limited *ab initio* MD simulations due to their computational expense, Giberti and Hssanali[23] proposed that the GDI alone is insufficient for capturing the thermodynamic and dynamic aspects of proton affinity to the

interface; instead, they asserted that WCI analysis can provide essential additional information about the nature of these behaviors.

Based on these WCI-based findings, combined with what we know from our earlier research on the surface affinity of the hydrated excess proton, the present study has utilized MD simulations to more carefully examine the behavior of hydrated excess proton near the air-water interface. In this work, both definitions of the interface, GDI and WCI, were employed in the simulations to understand the relationship and correlations between between them, as well as the role of the instantaneous fluctuations of the interface and the behavior of the hydrated excess proton near that interface. The conclusion from our work is that both definitions of the interface (as well as the distance of the hydrated excess proton from the interface) yield essentially the same value for the free energy of stabilization of the excess proton at the interface, that the definitions of the two interfaces are highly correlated in this light, but that the WCI definition also leads to additional subtle features associated with the effects of the hydrated excess proton on the definition of the WCI interface.

The remainder of this chapter is organized as follows: Section 2.2 describes the methods we used in our simulations, as well as details of the simulation system setup; Section 2.3.1 describes our findings with respect to the surface affinity of hydrated excess proton for the GDI and WCI and demonstrated the high degree of correlation between the two interfaces, while Section 2.3.2 presents the impact of the excess proton structure on the location and curvature of the WCI. This chapter concludes with a discussion of the analysis we employed to compare the GDI and WCI results, implications for the understanding of the behavior of interfacial hydrated excess protons, a summary of our findings, and concluding remarks.

2.2 Methodology

The proton transport (PT) process is a combination of at two mechanisms: the vehicular transport of the hydronium cation and the Grotthuss shuttling. During Grotthuss shuttling the hydrogen bonds rearrange, while the covalent bonds of water molecules and hydronium cations break and reform. Accordingly, an accurate physical model of the PT process must capture any topological changes in chemical bonding in order to accurately reflect the essential physics associated with this process. Since in traditional MD methods the bonding topology remains static, such approaches fall short in elucidating the detailed behavior of hydrated excess protons in water and related aqueous environments. It should also be noted that while *ab initio* molecular dynamics (AIMD) is capable of describing the dynamically changing bonding topology, these simulations are still very challenging computationally for larger systems such as those necessary to simulate an interface, and also for free energy sampling, which requires long simulation times for convergence. Therefore, for this work we have utilized the multistate empirical valence bond (MS-EVB) method, which is able to account for changes in bonding topology during PT and is far less computationally demanding compared to AIMD. When using an MS-EVB model, the state of the system is described as a linear combination of "basis states", $|i\rangle$, each of which represents a possible bonding topology of the system. The basis states are then coupled with each other via off-diagonal elements in a Hamiltonian-like matrix and the ground state eigenvector is solved for on the fly in the MD, which facilitates a realistic description of the PT process at any given timestep, as well as the hydration structure of the excess proton. At each time step, the ground state eigenvector of the Hamiltonian gives the populations of each basis state, which are then used to calculate the atomistic forces by applying the Hellman-Feynman theorem. A more detailed description of the MS-EVB framework can be found in earlier publications.[15, 24] Several MS-EVB

models have been developed that are able to accurately describe the behavior of hydrated proton in various systems such as the air-water interface and proton exchange membranes,[18, 25] as well as biomolecular systems (see, e.g., Ref.[26]).

In the MS-EVB framework, the center of excess charge (CEC) of the hydrated excess proton charge defect is used to represent the continuous and time-dependent location of the charge defect created by an excess proton. The CEC is a weighted average of the atomic coordinates of the protons in each basis state, defined as:

$$\boldsymbol{r}_{CEC} = \sum_{i=1}^{N} c_i^2 \, \boldsymbol{r}_{COC}^{i} \tag{2.1}$$

in which $\boldsymbol{r}_{COC}^{i}$ is the center of charge of the hydronium cation in the *i*-th eigenstate and c_i is the probability amplitude of that MS-EVB state, all as a function of the instantaneous point in time *t* of an MS-EVB trajectory. In this research we employed the MS-EVB 3.2 model, the details and parameters of which have been discussed in a previous publication.[27] When we refer here and in other literature to "the hydrated excess proton CEC", "the excess proton CEC", or just "the CEC", it is important to recognize that multiple protons in the hydrated proton structure participate in the CEC definition by virtue of Equation 2.1. The CEC is the middle of the overall net positive charge defect created by having an excess proton in the system (an electron "hole", by another point of view). The fact that multiple protons participate in the definition of the CEC in Equation 2.1 at any given instant is a manifestation of Grotthuss proton shuttling between the water molecules in the system.

For the present MS-EVB simulations of the air-water interface, the system was constructed as a slab of water consisting of 999 water molecules and 1 hydronium cation with vacuum on either side. The simulation cell was periodic in all directions with dimensions of 25 × 25 × 85 $Å^3$. The

depth of the water slab was ~ 45Å in the z-direction, leaving ~ 20Å of vacuum both above and below the water slab. The simulations were carried out with a modified version[28-29] of the LAMMPS MD software.[30] The long-range electrostatic interactions were calculated using the particle-particle-particle-mesh (PPPM) method with relative error set to 10^{-5}. All simulations were conducted in a constant *NVT* ensemble with a Nosé–Hoover thermostat having a relaxation constant of 200 fs.

We first established the initial configuration of the water slab with PACKMOL[31] and then equilibrated it using classical MD method 10 nanoseconds (ns); umbrella sampling was utilized for the production runs. The excess proton CEC was restrained at distances of 10-24 Å in the z-direction from the center of mass (COM) of the water slab in 29 evenly spaced windows. The force constant of the restraining potential was 5.0 kcal/mol/Å^2. For each window, 5 ns trajectories of production data were collected.

In order to compare and verify our conclusions, DFT-based AIMD simulations were also carried out for a similar system, although on a smaller scale. The water slab for the AIMD simulation consisted of 216 water molecules, 1 excess proton, and 1 chloride anion, and was placed in a periodic simulation box with dimensions of 15 × 15 × 77 Å^3. The depth of the AIMD water slab was ~37 Å, leaving ~20Å of vacuum above and below. The AIMD simulations were carried out with BLYP functional with Grimme dispersion correction[32] using a TZV2P basis set. Similar to the MS-EVB simulations, umbrella sampling was employed for free energy sampling. The AIMD simulations were carried out with CP2K[33] and a modified version of PLUMED.[34-36] The CEC was restrained at distances of 7-16 Å in the z-direction from the COM in 19 evenly spaced windows. The force constant for the restraint was set to 10.0 kcal/mol/Å^2. For each window, 50 ps of trajectory was obtained.

2.3 Results and Discussions

2.3.1 Surface Affinity of the Hydrated Excess Proton

To evaluate the differences and similarities of interfacial proton behavior with respect to static (GDI) and instantaneous (WCI) interfaces, two collective variables (CVs) were constructed. The CV-GDI is the distance from the excess proton CEC to the GDI; a positive value indicates that the CEC is on the bulk side of the interface, while a negative value indicates that it is beyond the interface and is on the vacuum side. For this study, we determined the GDI be a plane normal to the z-axis of the simulation box located where local water density is 0.016 $Å^{-3}$, half of the number density of bulk water under 298K (0.032 $Å^{-3}$).

The CV-WCI represents the distance from the excess proton CEC to the WCI, for which the positive and negative values convey similar meanings to that of CV-GDI. However, instead of local density used in the GDI, the WCI uses a normalized Gaussian function for particles in a system, given by

$$\phi(\boldsymbol{r}; b) = (2\pi b^2)^{-d/2} \exp\left(-\frac{r^2}{2b}\right) \tag{2.2}$$

where d is the dimensionality of the system and b is the bandwidth of the Gaussian density function, which should be selected according to the physical conditions of the system under consideration. In this study, we set d = 3 and used $b = 2.4$ Å, which is roughly the diameter of one water molecule and is consistent with the original article proposing WCI.[19] From Equation 2.2, the density field of any given point in space at a certain time step can be written as:

$$\bar{\rho}(\boldsymbol{r}, t) = \sum_i \phi(|\boldsymbol{r} - \boldsymbol{r_i}(t)|; b) \tag{2.3}$$

The WCI is the $(d-1)$-dimensional manifold $\boldsymbol{r} = \boldsymbol{s}$ such that:

$$\bar{\rho}(\boldsymbol{s}, t) \equiv c \tag{2.4}$$

where c is a constant. For this study, c was set to 0.016 Å^{-3}, which is one-half of the bulk water density and consistent with calculating the GDI. Thus, the WCI in this study can be viewed as a 2D-surface describing the instantaneous shape of the water-air interface.

The potential of mean force (PMF) for each collective variable was calculated according to the weighted histogram analysis method (WHAM),[37] as shown in Figure 2.1. Importantly, the two CVs showed the same general behavior for both MS-EVB and AIMD simulations, confirming that a hydrated excess proton tends to reside near the interface regardless of which definition of the interface is chosen. Moreover, the width and the depth of the energy well shown in the two PMF figures are consistent with each other and for both simulation methods, again indicating a very similar magnitude of proton affinity for these two interfaces.

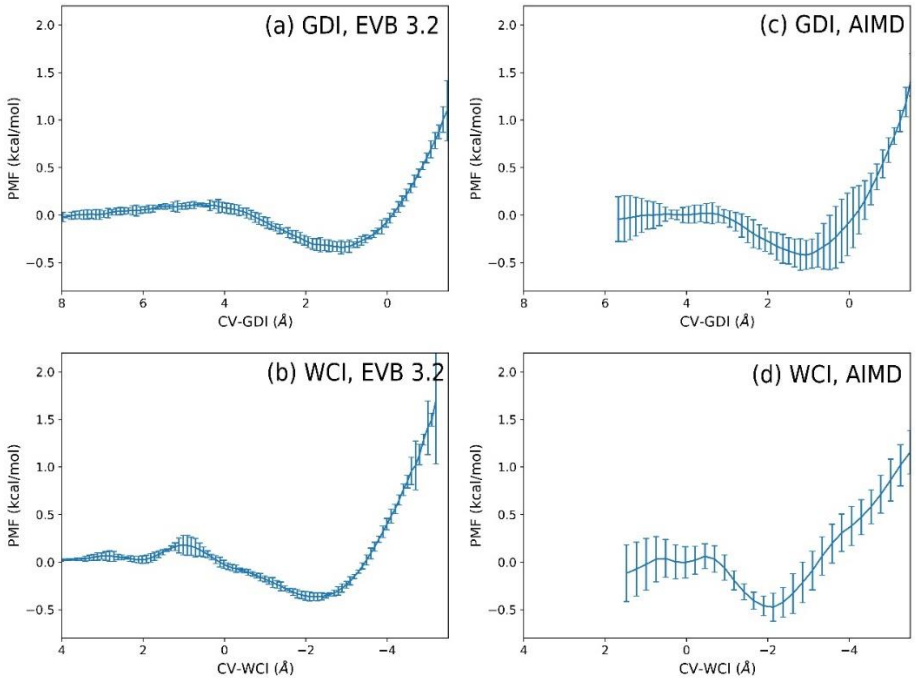

Figure 2.1 (a) 1D PMF of the CV-GDI with EVB 3.2; (b) 1D PMF of the CV-WCI with EVB 3.2; (c) 1D PMF of the CV-GDI with AIMD; (d) 1D PMF of the CV-WCI with AIMD. The two CVs show a very similar trend and magnitude for the surface affinity of the excess proton, and the MS-EVB 3.2 results are consistent with the AIMD results.

To develop a more comprehensive understanding of the relationship (and correlation) between the two CVs, a full 2D PMF was calculated using the WHAM-2D method, as shown in Figure 2.2; this 2D PMF was calculated with EVB 3.2 results to obtain better convergence. The two 1D PMFs were aligned along their corresponding axes for reference. The centers of the energy wells of the two 1D PMFs align in the energy minimum of the 2D PMF, thus revealing a very high correlation between the two CVs.

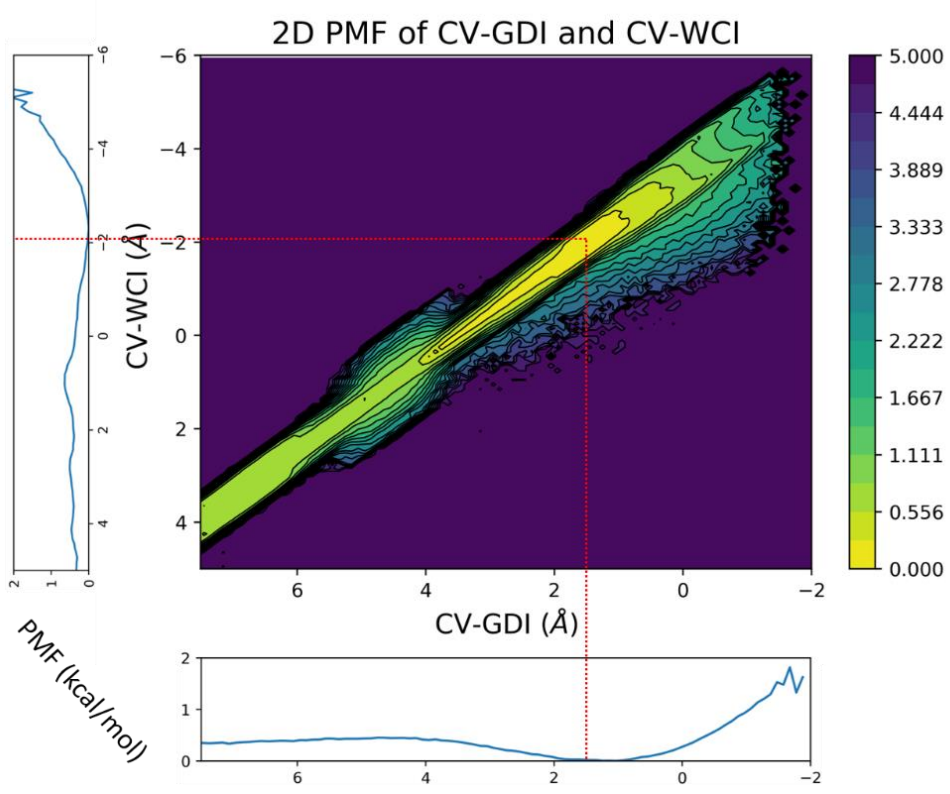

Figure 2.2 2D PMF of CV-GDI (x axis) and CV-WCI (y axis). The two 1D PMFs are placed along their axes for reference (Note that the zero of the PMFs in these figures is set at their minimum, unlike the PMF depiction in Fig. 2.1, where the PMF zero is taken to be the bulk region). The red dotted lines denote the minimum values of the PMFs.

To further understand the process whereby the excess proton moves from the liquid phase across the interface, we utilized the finite-temperature string method[38-39] to calculate the minimum

free energy path (MFEP) in the two collective variables. With a set of CVs to describe a reaction, the MFEP is defined as the reaction path of maximum likelihood in these CVs; moreover, the MFEP is expected to represent the center of the reactive trajectories and indicate the most probable reaction path.[39] Our MFEP results are illustrated in Fig. 2.3. In Figure 2.3(a), the MFEP shows a similar trend and shape to the 1D PMFs of both CV-GDI and CV-WCI. At the minimal point of the MFEP, we found CV-GDI = 0.998 Å and CV-WCI = -2.502 Å, both of which are consistent with the minimal points in the 1D PMFs. As indicated in Figure 2.3(b), the almost straight red line denotes the MFEP of the 2D CV space. Note that the two CVs are thus nearly perfectly correlated along the reactive trajectory, which confirms that the surface affinity of excess proton is not dependent on whether GDI or WCI is the designated interface. Based on the fact that our results for CV-GDI and CV-WCI were similar, hereafter we mainly show data for only the CV-GDI.

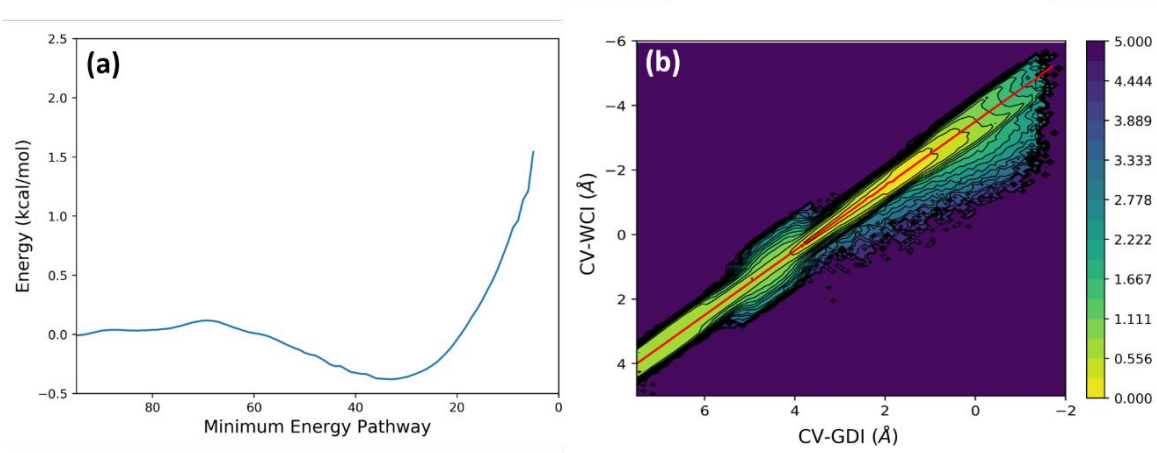

Figure 2.3 (a) MFEP from the CV-GDI and the CV-WCI. The x-axis denotes the "image" index, and the y-axis denotes the corresponding free energy. The "images" are evenly spaced representative points on the MFEP and each represents a state in the CV space - e.g. the minimum point (image 36) denotes a state where CV-GDI = 0.998 Å and CV-WCI = -2.502 Å. (b) MFEP (solid red line) plotted on 2D PMF of the two CVs.

2.3.2 Interfacial Solvation Structure of the Hydrated Excess Proton

A hydrated excess proton is usually described as two limiting structures: a Zundel cation $H_5O_2^+$ and an Eigen cation $H_9O_4^+$. Prior studies have indicated that an excess proton migrates through the hydrogen bond network from one water molecule to another via Grotthuss hopping in an Eigen-Zundel-Eigen hop sequence.[40] To determine if the excess proton is more Eigen-like or Zundel-like at a given MD time step, two characteristic variable can be introduced: δ and ξ, both of which are useful for determining the magnitude of charge delocalization. δ is calculated as:

$$\delta = \left| d_{O^*H} - d_{O_WH} \right| \tag{2.5}$$

where d_{O^*H} is the distance between the shared hydrogen atom and the hydronium oxygen, and d_{O_WH} is the distance between the shared hydrogen atom and the water oxygen atom. Note that both the shared hydrogen atom and the water oxygen are from the "special pair" of the hydronium. A smaller δ indicates that the charge is more delocalized, and the hydrated excess proton structure is more Zundel-like, and vice-versa. On the other hand, ξ is calculated as:

$$\xi = c_1^2 - c_2^2 \tag{2.6}$$

where c_1 and c_2 are the probability coefficients of the two most likely MS-EVB states. A smaller ξ denotes the likelihood that the two states are close, pointing to more delocalization and a Zundel-like cation. Both δ and ξ were calculated and plotted in separate 2D PMFs of the CV-GDI, as shown in Fig 2.4. The behavior of both variables indicates that regardless of whether the excess proton is in the bulk or interfacial/vacuum region, the charge delocalization behavior remains consistent between the two variable definitions, as shown by the fact that the minimal point of δ and ξ behaved very similarly when moving along the axis of the CV-GDI. The results also show that at the air-water interface (a GDI value of around 1.0) the hydrated excess proton structure exhibits greater fluctuations to visit the Zundel cation $H_5O_2^+$ and $H_7O_3^+$ limiting structures than

when in the bulk water region. (Note that since neither δ or ξ were directly biased in the simulations, more sampling was required to reach good convergence of the 2D PMFs; hence, the 2D PMFs were calculated based on MS-EVB 3.2 results which displayed good consistency with the AIMD results reported earlier.)

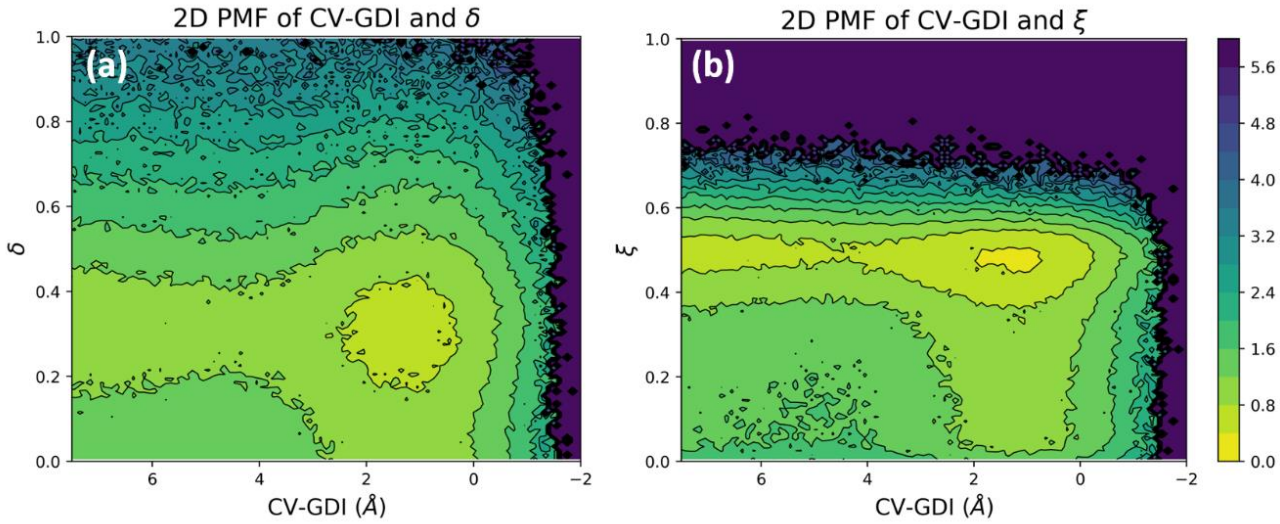

Figure 2.4 (a) 2D PMF of $\boldsymbol{\delta}$ and CV-GDI. (b) 2D PMF of $\boldsymbol{\xi}$ and CV-GDI.

To evaluate solvation structure of the hydrated excess proton, we utilized a continuous soft coordination number[41-42] of water oxygens to the hydronium oxygen. Figure 2.5 shows the 2D PMF of the coordination number and the CV-GDI. The lowest-energy and most probable coordination number was noted to be 3.0 (the Eigen cation, $H_9O_4^+$), regardless of the location of the excess proton; this finding indicates that the first solvation shell remains intact, forming the protonated water complex. This water complex persisted even when the excess proton migrated into a low-density interfacial region, although greater fluctuations to the range 2.0-2.5 are seen in that region (more Zundel-like and $H_7O_3^+$ character, as also seen in Fig. 2.4). Note that a protonated cluster of water molecules in the interfacial region forms a local high-density bubble that can alter

the overall density field and impact the calculation of WCI, which we will discuss next. This robust solvation structure also explains the unchanged magnitude of charge delocalization along CV-GDI, as shown in Figure 2.4.

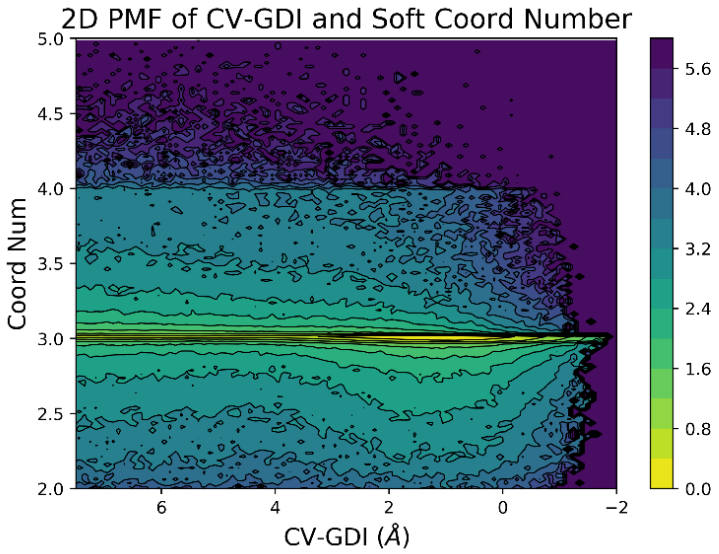

Figure 2.5 2D PMF of soft coordination number and CV-GDI

To understand the impact that this water cluster might have on the WCI, we calculated the mean curvature of the WCI at the nearest point to the excess proton CEC. Mathematically, the mean curvature is defined as the average of the two principal curvatures of the surface. In this study, a positive mean curvature indicates that the WCI is protruding into the vacuum, while a negative mean curvature denotes that the WCI is indenting into the bulk region. Figure 2.6 shows the 2D PMF of the mean curvature and the CV-WCI. As shown therein, after moving past the WCI towards the vacuum, the protonated water complex begins to pull the WCI outward, forming a broad peak in the mean curvature on the 2D PMF.

The interaction between the protonated water cluster and the WCI can firstly explain the somewhat weakening correlation observed in the 2D PMF in Figure 2.2 while moving past the

minimum into the more vacuum region. Secondly, the CV-WCI and CV-GDI mostly correlate very well when the excess proton is in the bulk region, but as the hydrated excess proton moves into the bulk region the correlation of the two CVs also weakens in this region for the GDI between 4 and 6 Å (see Fig 2.2). Interestingly, this weakening correlation can be separated into two stages that display different patterns in the 2D PMF of Fig 2.2. The first stage corresponds to when the CV-WCI is approximately -1 Å to 1 Å, during which the hydronium and its first solvation shell are roughly at the location of the WCI. This water cluster creates a relatively high-density bubble, due to hydrogen bond contractions to the hydronium core, compared with the surrounding interfacial environment, thereby impacting the calculation of the density field, which in turn affects the resulting WCI coordinates. Since the CV-WCI refers to the distance between the excess proton (CEC) and the WCI, this CV becomes increasingly self-interactive, resulting in a wider distribution with both an upside tail and a downside tail. In contrast, the second stage of the weakening correlation occurs when the CV-WCI is greater the 1 Å. At this point the excess proton is beyond the WCI and the charged water cluster pulls the WCI towards the excess proton, resulting in a widened distribution with a tail only on the downside.

Based on the simulation data that has emerged from the present study, we can conclude that both the instantaneous interface (WCI) and the average interface (GDI) afford the same outcome with respect to the surface affinity of the hydrated excess proton. However, while the WCI accounts for the instantaneous fluctuations of the interface, it is more computationally demanding and can be influenced by the coordinates of the excess proton.

In a recent study, Das et al. also confirmed the aforementioned surface affinity of excess proton, both for the WCI and GDI,[11] using AIMD simulation. However, these authors further claimed that the hydrated excess proton is stabilized by the negative counterion at the interface, a

conclusion they based on the fact that the radial distribution function (RDF) for the hydronium oxygen and the counterion displayed a higher first peak at the interface. By contrast, the results of our simulations here provide no similar support for this conclusion. Based on both MS-EVB 3.2 and AIMD simulations, our 1D PMFs show free energy wells at the interface, which are comparable to the Das et al. results. However, in our MS-EVB 3.2 simulations the counterion was not present and the excess charge was balanced with a uniform neutralizing background. It should also be noted that in our AIMD simulations the counterion showed little to no presence within 6 Å of the excess proton over the simulated time span. These data suggest that the counterion does not play an essential role in the surface affinity of the hydrated excess proton. Similarly, Chiang et al. [12] reported that the surface absorption of excess proton is independent of any specific proton-halide anion interaction, which is consistent with our findings.

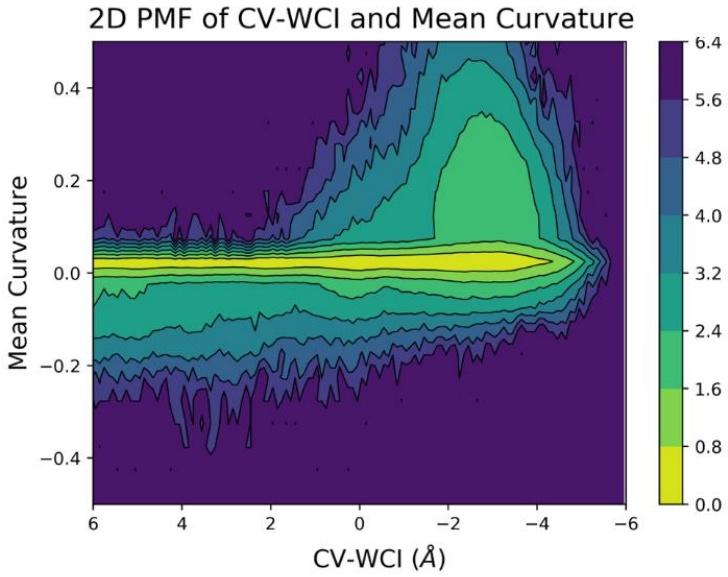

Figure 2.6 2D PMF of the mean curvature and the CV-WCI

2.3.3 Additional Simulations with Counter-ion Present

As detailed in previous sections, our EVB 3.2 simulations were set up in the absence of the counterion, and the excess charge introduced by excess proton was balanced with a uniform neutralizing background. To further understand the role of the counterion in this system, additional simulations with a chloride anion as the counterion were conducted. The simulations were set up with the same procedures, compositions, and parameters with that of the simulations in the main text, except that one counterion is added in the system to balance the excess proton. The CEC was restrained at distances of 10-24Å in the z-direction from the center of mass (COM) of the water slab in 15 evenly spaced windows. The force constant of the restraining potential was 5.0 kcal/mol/Å^2. For each window, 3 ns trajectories of production data were collected.

For each window, the radial distribution function (RDF) between the center of excess proton (CEC) and the chloride anion was plotted, as shown in Figure 2.7. The number in the legend of the figure denotes distances between the center of umbrella potential and the GDI. Larger numbers (red lines) represent RDF results of bulk-like umbrella windows and smaller numbers (blue lines) represent interfacial RDF results. Notice that there is no clear trend of heightening or lowering of first peak in the RDF figures, as the center of the umbrella window moving from the bulk region towards the interface. The binding between the counterion and the excess proton does not show a consistent trend with respect to the solvation environment of the excess proton.

We then examined the effect of the counterion on the surface solvation of excess proton. Figure 2.8 compares the PMF of CV-GDI with and without the counterion. As shown in the two figures, there is no apparent difference on the shape of PMF and the depth of energy barrier whether the counterion is present or not. Based on these findings, and the fact that in AIMD

simulations the excess proton and the counterion rarely come near to each other, the counterion does not seem to play an important role in stabilizing the excess proton near the interface.

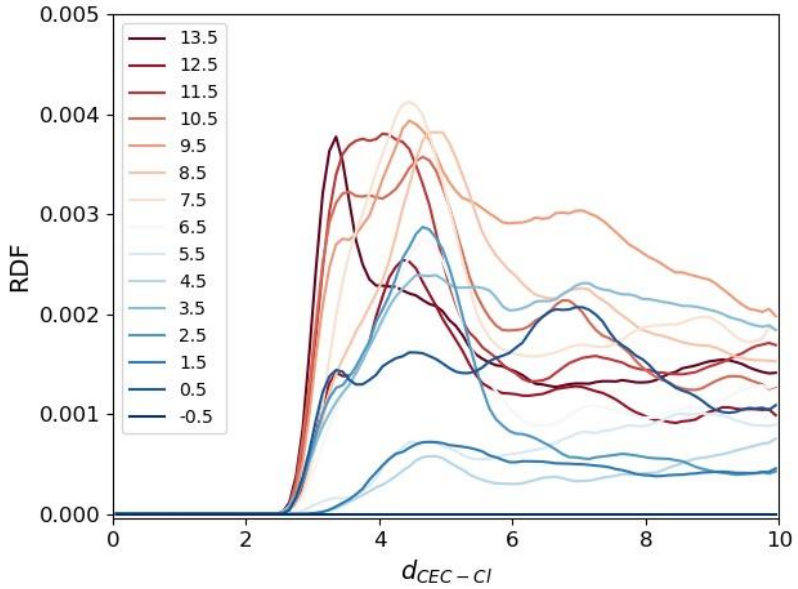

Figure 2.7 Interfacial vs bulk RDF between CEC and chloride anion. The numbers in the legend denotes distances between the center of umbrella potential and the GDI. Larger numbers (red lines) represent RDF results of bulk-like umbrella windows and smaller numbers (blue lines) represent interfacial RDF results.

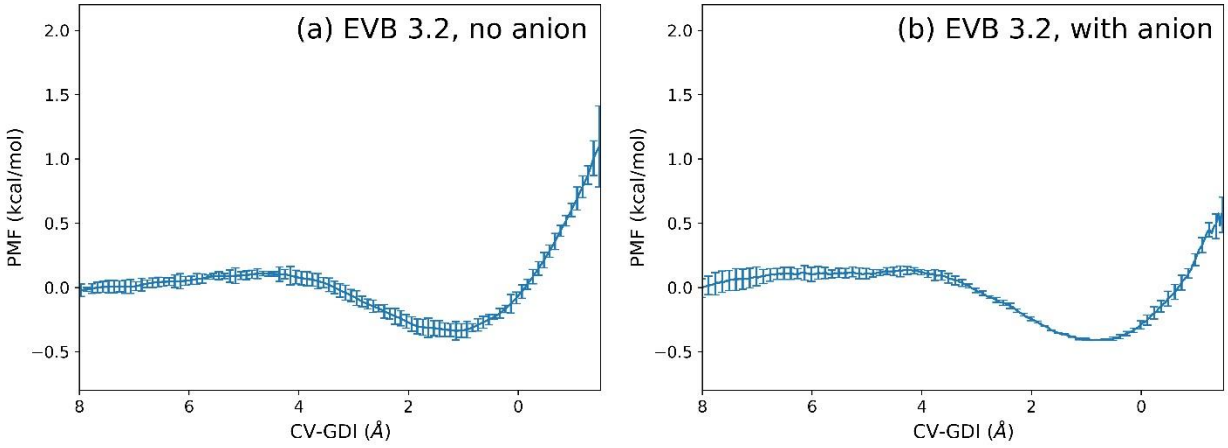

Figure 2.8 PMF of CV-GDI with and without counterion.

2.4 Conclusions

This study was designed to investigate the interfacial behavior of a hydrated excess proton with respect to two different definitions of interface using both thee MS-EVB method and DFT-based AIMD. As detailed herein, the GDI and WCI afforded similar results demonstrating that the excess proton tends to reside at the interface for either CV; moreover, our EVB 3.2 and AIMD results are broadly consistent with one another. A composite 2D PMF constructed from the two CV definitions of interface showed a high degree of good correlation between the results of two CVs, with that correlation somewhat weakening when the excess proton moves near and past the interface. We attribute this weakened correlation beyond the interface to the charged water cluster formed around the excess proton that interrupts the interfacial density field, which in turn influences the location and shape of the WCI. Due to its dependence on the coordinates of the CEC of the hydrated excess proton, the WCI has difficulty disentangling the interfacial thermodynamics of the excess proton from the influence on the surface curvaturs induced by the excess proton itself. This work reaffirms the likelihood that the hydrated excess proton has an affinity for the air-water interface no matter how that interface is defined – a result that is consistent with the original prediction made in sixteen years ago[3] and now supported by a significant body of experimental results, include two very recent studies.[11-12]

2.5 References

1. Baer, M. D.; Kuo, I. F. W.; Tobias, D. J.; Mundy, C. J., Toward a Unified Picture of the Water Self-Ions at the Air-Water Interface: A Density Functional Theory Perspective. *Journal of Physical Chemistry B* **2014**, *118*, 8364-8372.

2. Jungwirth, P.; Tobias, D. J., Specific Ion Effects at the Air/Water Interface. *Chemical Reviews* **2006**, *106*, 1259-1281.

3. Petersen, M. K.; Iyengar, S. S.; Day, T. J. F.; Voth, G. A., The Hydrated Proton at the Water Liquid/Vapor Interface. *Journal of Physical Chemistry B* **2004**, *108*, 14804-14806.

4. Petersen, P. B.; Saykally, R. J., Evidence for an Enhanced Hydronium Concentration at the Liquid Water Surface. *Journal of Physical Chemistry B* **2005**, *109*, 7976-7980.

5. Tarbuck, T. L.; Ota, S. T.; Richmond, G. L., Spectroscopic Studies of Solvated Hydrogen and Hydroxide Ions at Aqueous Surfaces. *Journal of the American Chemical Society* **2006**, *128*, 14519-14527.

6. Levering, L. M.; Roxana Sierra-Hernández, M.; Allen, H. C., Observation of Hydronium Ions at the Air-Aqueous Acid Interface: Vibrational Spectroscopic Studies of Aqueous Hcl, Hbr, and Hi. *Journal of Physical Chemistry C* **2007**, *111*, 8814-8826.

7. Tian, C.; Ji, N.; Waychunas, G. A.; Shen, Y. R., Interfacial Structures of Acidic and Basic Aqueous Solutions. *Journal of the American Chemical Society* **2008**, *130*, 13033-13039.

8. Das, S.; Bonn, M.; Backus, E. H. G., The Surface Activity of the Hydrated Proton Is Substantially Higher Than That of the Hydroxide Ion. *Angewandte Chemie International Edition* **2019**, *58*, 15636-15639.

9. Mucha, M.; Frigato, T.; Levering, L. M.; Allen, H. C.; Tobias, D. J.; Dang, L. X.; Jungwirth, P., Unified Molecular Picture of the Surfaces of Aqueous Acid, Base, and Salt Solutions. *Journal of Physical Chemistry B* **2005**, *109*, 7617-7623.

10. Ishiyama, T.; Morita, A., Molecular Dynamics Analysis of Interfacial Structures and Sum Frequency Generation Spectra of Aqueous Hydrogen Halide Solutions. *Journal of Physical Chemistry A* **2007**, *111*, 9277-9285.

11. Das, S.; Imoto, S.; Sun, S.; Nagata, Y.; Backus, E. H.; Bonn, M., Nature of Excess Hydrated Proton at the Water-Air Interface. *Journal of the American Chemical Society* **2019**, *142*, 945-952.

12. Chiang, K.-Y.; Dalstein, L.; Wen, Y.-C., Affinity of Hydrated Proton at Intrinsic Water/Vapor Interface Revealed by Ion-Induced Water Alignment. *Journal of Physical Chemistry Letters* **2020**, *11*, 696-701.

13. Iuchi, S.; Chen, H.; Paesani, F.; Voth, G. A., Hydrated Excess Proton at Water-Hydrophobic Interfaces. *Journal of Physical Chemistry B* **2009**, *113*, 4017-4030.

14. Kumar, R.; Knight, C.; Voth, G. A., Exploring the Behaviour of the Hydrated Excess Proton at Hydrophobic Interfaces. *Faraday Discussions* **2013**, *167*, 263-278.

15. Schmitt, U. W.; Voth, G. A., The Computer Simulation of Proton Transport in Water. *Journal of Chemical Physics* **1999**, *111*, 9361-9381.

16. Day, T. J. F.; Soudackov, A. V.; Čuma, M.; Schmitt, U. W.; Voth, G. A., A Second Generation Multistate Empirical Valence Bond Model for Proton Transport in Aqueous Systems. *Journal of Chemical Physics* **2002**, *117*, 5839-5849.

17. Wu, Y.; Chen, H.; Wang, F.; Paesani, F.; Voth, G. A., An Improved Multistate Empirical Valence Bond Model for Aqueous Proton Solvation and Transport. *Journal of Physical Chemistry B* **2008**, *112*, 467-482.

18. Tse, Y. L. S.; Chen, C.; Lindberg, G. E.; Kumar, R.; Voth, G. A., Propensity of Hydrated Excess Protons and Hydroxide Anions for the Air-Water Interface. *Journal of the American Chemical Society* **2015**, *137*, 12610-12616.

19. Biswas, R.; Tse, Y. L. S.; Tokmakoff, A.; Voth, G. A., Role of Presolvation and Anharmonicity in Aqueous Phase Hydrated Proton Solvation and Transport. *Journal of Physical Chemistry B* **2016**, *120*, 1793-1804.

20. Agmon, N., The Grotthuss Mechanism. *Chemical Physics Letters* **1995**, *244*, 456-462.

21. Willard, A. P.; Chandler, D., Instantaneous Liquid Interfaces. *Journal of Physical Chemistry B* **2010**, *114*, 1954-1958.

22. Wick, C. D., Comparing Hydroxide and Hydronium at the Instantaneous Air-Water Interface Using Polarizable Multi-State Empirical Valence Bond Models. *Computational and Theoretical Chemistry* **2017**, *1116*, 64-72.

23. Giberti, F.; Hassanali, A. A., The Excess Proton at the Air-Water Interface: The Role of Instantaneous Liquid Interfaces. *Journal of Chemical Physics* **2017**, *146*, 244703.

24. Knight, C.; Lindberg, G. E.; Voth, G. A., Multiscale Reactive Molecular Dynamics. *Journal of Chemical Physics* **2012**, *137*, 22A525.

25. Arntsen, C.; Savage, J.; Tse, Y. L. S.; Voth, G. A., Simulation of Proton Transport in Proton Exchange Membranes with Reactive Molecular Dynamics. *Fuel Cells* **2016**, *16*, 695-703.

26. Liang, R.; Swanson, J. M. J.; Wikström, M.; Voth, G. A., Understanding the Essential Proton-Pumping Kinetic Gates and Decoupling Mutations in Cytochrome C Oxidase. *Proceedings of the National Academy of Sciences* **2017**, *114*, 5924-5929.

27. Biswas, R.; Tse, Y. L. S.; Tokmakoff, A.; Voth, G. A., Role of Presolvation and Anharmonicity in Aqueous Phase Hydrated Proton Solvation and Transport. *Journal of Physical Chemistry B* **2016**, *120*, 1793-1804.

28. Yamashita, T.; Peng, Y.; Knight, C.; Voth, G. A., Computationally Efficient Multiconfigurational Reactive Molecular Dynamics. *Journal of chemical theory and computation* **2012**, *8*, 4863-4875.

29. Peng, Y.; Knight, C.; Blood, P.; Crosby, L.; Voth, G. A., Extending Parallel Scalability of Lammps and Multiscale Reactive Molecular Simulations. *Proceedings of the 1st Conference of the Extreme Science and Engineering Discovery Environment: Bridging from the eXtreme to the campus and beyond* **2012**, 1-7.

30. Plimpton, S.; Crozier, P.; Thompson, A., Lammps-Large-Scale Atomic/Molecular Massively Parallel Simulator. *Sandia National Laboratories* **2007**, *18*, 43.

31. Martinez, L.; Andrade, R.; Birgin, E. G.; Martínez, J. M., Packmol: A Package for Building Initial Configurations for Molecular Dynamics Simulations. *Journal of Computational Chemistry* **2009**, *30*, 2157-2164.

32. Grimme, S., Accurate Description of Van Der Waals Complexes by Density Functional Theory Including Empirical Corrections. *Journal of Computational Chemistry* **2004**, *25*, 1463-1473.

33. Hutter, J.; Iannuzzi, M.; Schiffmann, F.; Vandevondele, J., Cp2k: Atomistic Simulations of Condensed Matter Systems. *Wiley interdisciplinary reviews: Computational molecular science* **2014**, *4*, 15-25.

34. Bonomi, M., et al., Promoting Transparency and Reproducibility in Enhanced Molecular Simulations. *Nature Methods* **2019**, *16*, 670-673.

35. Bonomi, M., et al., Plumed: A Portable Plugin for Free-Energy Calculations with Molecular Dynamics. *Computer Physics Communications* **2009**, *180*, 1961-1972.

36. Tribello, G. A.; Bonomi, M.; Branduardi, D.; Camilloni, C.; Bussi, G., Plumed 2: New Feathers for an Old Bird. *Computer Physics Communications* **2014**, *185*, 604-613.

37. Kumar, S.; Rosenberg, J. M.; Bouzida, D.; Swendsen, R. H.; Kollman, P. A., The Weighted Histogram Analysis Method for Free-Energy Calculations on Biomolecules. I. The Method. *Journal of computational chemistry* **1992**, *13*, 1011-1021.

38. E, W.; Ren, W.; Vanden-Eijnden, E., Finite Temperature String Method for the Study of Rare Events. *Journal of Physical Chemistry B* **2005**, *109*, 6688-6693.

39. Maragliano, L.; Fischer, A.; Vanden-Eijnden, E.; Ciccotti, G., String Method in Collective Variables: Minimum Free Energy Paths and Isocommittor Surfaces. *Journal of Chemical Physics* **2006**, *125*, 024106.

40. Markovitch, O.; Chen, H.; Izvekov, S.; Paesani, F.; Voth, G. A.; Agmon, N., Special Pair Dance and Partner Selection: Elementary Steps in Proton Transport in Liquid Water. *Journal of Physical Chemistry B* **2008**, *112*, 9456-9466.

41. Iannuzzi, M.; Laio, A.; Parrinello, M., Efficient Exploration of Reactive Potential Energy Surfaces Using Car-Parrinello Molecular Dynamics. *Physical Review Letters* **2003**, *90*, 238302.

42. White, A. D.; Voth, G. A., Efficient and Minimal Method to Bias Molecular Simulations with Experimental Data. *Journal of Chemical Theory and Computation* **2014**, *10*, 3023-3030.

CHAPTER 3

INTERFACIAL SOLVATION AND SLOW TRANSPORT OF HYDRATED EXCESS PROTONS IN THE NON-IONIC REVERSE MICELLES

Reproduced from Li, Z., & Voth, G. A. (2020). *Physical Chemistry Chemical Physics*, 22(19), 10753-10763.with permission from the PCCP Owner Societies.

3.1 Introduction

Proton transport (PT) in confined regions occurs in systems ranging from proton exchange membranes[1-6] to various biological systems (see, e.g., Refs[7-11]) Our previous studies on interfacial hydrated excess protons[12-16] predict that the PT process is significantly different in interfacial systems compared to how it behaves in the bulk. An interfacial preference for the hydrated excess proton (hydronium-like cation) was predicted as early as 2004.[12] Our prior study of lipid bilayer interfaces[15] also revealed that excess protons tend to form a distorted Zundel cation in the interfacial region. In a related study, Wolf *et al.*[17] also modeled that excess protons exhibit interface affinity near the DMPC membrane. Moreover, Zhang *et al.*[18] found from ab initio MD simulation that a hydrated excess proton tends to locate near an apolar hydrophobic interface, consistent with our earlier predictions.[12-15] These findings point to the importance of understanding the behavior and interfacial effects of hydrated protons in confined and interfacial systems.

Reverse micelles are amphiphilic structures that spontaneously form when surfactants are dissolved into non-polar solvents. A nanoscale water pool forms, which is surrounded by the hydrophilic head groups of the surfactant molecules. This resulting confinement alters both the

structural and dynamical properties of the water pool compared to more conventional (e.g., bulk) systems. The thermodynamic and spectroscopic properties of reverse micelle systems have been studied with a variety of experimental techniques, including IR and Raman spectroscopy,[19-20] NMR,[21] fluorescence probe,[22-23] etc. These efforts help to reveal the microscopic details of the confined water pool in a reverse micelle, which is usually portrayed as a roughly spherical shape that can be divided into two regions: (1) the interfacial region, in which both rotational and translational motions of water molecules are known to be largely immobilized; and (2) the central region, where the confinement effect is less severe and water molecules behave somewhat similar to the bulk system. However, the existence and nature of both regions depends on the size of the micellar water pool under consideration. In cases where the micellar water pools size is relatively small, the central region can be incomplete or even absent; in such instances all water molecules in the pool exhibit interfacial traits.

Recent work by Van der Loop et al.[24] applied GHz dielectric relaxation spectroscopy to non-ionic reverse micelle systems, which has provided further experimental evidence of the altered PT behavior in reverse micelles. They attributed this phenomenon to a collective slowing down of water dynamics. Earlier theoretical studies on reverse micelles[25-26] and nanometer-scale water droplets[27] suggest that the interfacial solvation of the hydrated excess proton is responsible for slow proton diffusion. Based on what is already known about the interfacial affinity of excess proton,[12, 15, 17-18] our present study was designed to examine the behavior of PT in reverse micelles with neutral head groups. More specifically, we investigated the solvation and transport of hydrated excess proton dissolved in micellar water pools of various sizes encapsulated by non-ionic surfactant molecules.

The rest of the chapter is organized as follows: Section 3.2 describes the methods we used in our simulations, as well as details about our simulation system setup. Section 3.3 describes our findings about the equilibrium structure of reverse micelles, micellar solvation of the excess protons, and slow proton transport of those micellar excess proton. The chapter concludes with a discussion of the analysis we employed to understand the slow transport of hydrated excess proton, a review of our findings, and closing observations in Section 3.4.

3.2 Methodology

Igepal CO-520 surfactant was used to construct the reverse micelles, which contain ether and hydroxyl oxygen atoms in their hydrophilic head groups. Hereafter, the hydroxyl group oxygen will be referred to as OHyx and ether oxygen atoms as OEther. The structure of the surfactant is show in Figure 3.1. The pK_b of the head group in Igepal surfactants is found to be ~16 to 18, making it unlikely for excess proton to protonate the head group. Further, based on experimental results[28-29] and earlier simulations of methanol-water mixtures,[30] the presence of protonated alcohol oxygen is negligible compared to hydronium cations (H_3O^+) and therefore can be safely disregarded.

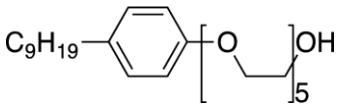

Figure 3.1 Structure of Igepal CO-520 surfactant molecule. Note that oxygen atoms in the hydroxyl group will be referred to as OHyx; and ether oxygen atoms will be referred to as OEther.

Reverse micelles of four sizes were constructed corresponding to the diameters of the water pool: 1nm, 2nm, 4nm, and 6nm. Experimentally, a ratio w_0 = [H_2O]/[surfactant] is generally used to provide an estimate of the size of the water pool in the reverse micelles. In our setup, the number

of water molecules in each system was determined with the desired volume of the water pool and bulk water density at 298K. The number of surfactant molecules encapsulating the water pool was initially estimated from w_0 and then adjusted by examining the trajectories from classical MD simulations. The remainder of the simulation box was filled with cyclohexane molecules at a bulk density of 298K. Detailed compositions and final w_0 values for the reverse micelle systems can be found in Table 3.1. We defined the initial configurations of each systems using the PACKMOL[31] software package. The general Amber force field (GAFF)[32] was used to describe cyclohexane and surfactant molecules with RESP charges obtained via *ab initio* calculations carried out by R.E.D. server.[33-36] The LAMMPS MD software[37] and an anharmonic water model aSPC/Fw[38] were utilized for all simulations. The reverse micelles were first equilibrated with classical MD simulation for 5 ns in the constant *NPT* ensemble at 298K and 1 atm, and then another 5 ns in the constant *NVT* ensemble at 298K. Then, the water molecule closest to the center of mass (COM) of the water pool was replaced with a hydronium cation and a chloride anion, after which MS-RMD was applied in the NVE ensemble. For each micellar size, 5 statistically independent simulations were conducted, which resulted in a total of 15 ns of trajectories.

Table 3.1 Compositions of Reverse Micelle Systems

Water Pool Diameter	Number of Water	Number of Surfactant	w0
1nm	15	15	1.0
2nm	118	52	2.3
4nm	994	208	4.8
6nm	3186	468	6.8

3.3 Results and Discussion

3.3.1 Equilibrium Structure of Reverse Micelles

We first looked at specific intrinsic structural properties of these confined environments, which we surmised may impact the solvation of the excess proton charge. Recall that a reverse micelle represents an inhomogeneous environment, with a water pool surrounded by the hydrophilic head groups of surfactant molecules. For this inhomogeneous system, we applied a local density profile function to describe how the density varied as a function of distance from a reference point. With the center of mass of the water pool as the reference point, the local density of a species was defined as:[26]

$$\rho_{COM-\alpha} = \frac{1}{4\pi r^2}\langle \sum_{i=1}^{N} \delta(|r_i^{\alpha} - R_{COM}| - r)\rangle \tag{3.1}$$

in which R_{COM} is the COM coordinate, r_i^{α} denotes the coordinate of site α on the *i*-th molecule.

Figure 3.2 presents the local density profile of water oxygen (OW), OHyx, and OEther. Note that the OW plot uses the left y-axis and the surfactant atoms (OHyx and OEther) use the right y-axis. In each figure, the vertical black dashed line indicates the location of the Gibbs dividing surface (GDS), which represents an idealized, zero-volume plane to separate two phases. The GDS utilizes the local density of the target species and is defined as the surface where the local density is half of the bulk density. For this study, we decide the GDS locates at where local water density is 0.016 $Å^{-3}$, half of the number density of bulk water at 298K (0.032 $Å^{-3}$). For our reverse micelles, atoms in the surfactant hydrophilic head group (OHyx and OEther) both reached a significant local density at the GDS, which means the interface was a mixture of water molecules

and surfactant head groups, which is important since the head groups can play a role in interfacial excess proton behavior.

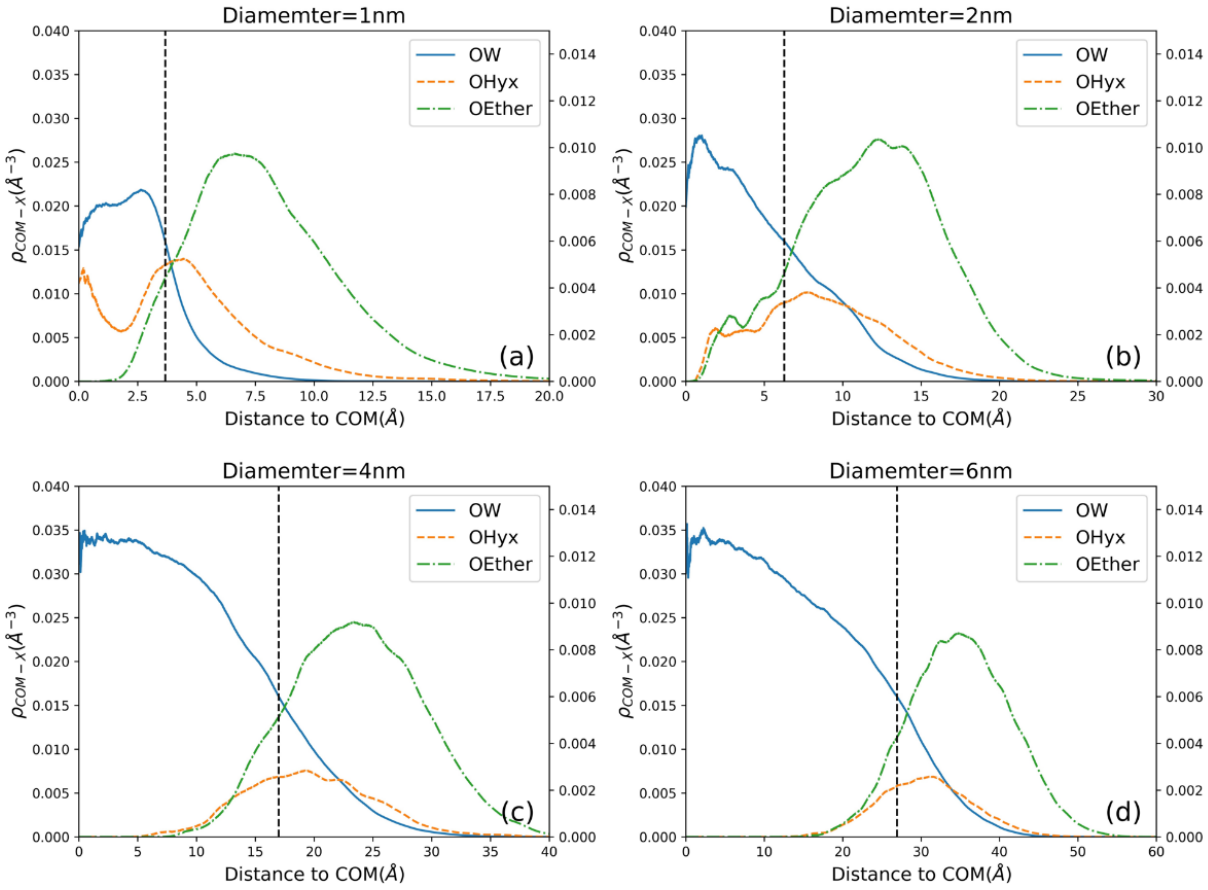

Figure 3.2 Local density profiles with COM of water pool as center of different micellar sizes: (a) diameter=1nm, (b) d=2nm, (c) d=4nm, and (d) d=6nm. OW: oxygen atom water molecule; OHyx: hydroxyl oxygen in surfactant head group; OEther: ether oxygen in surfactant head group

For the two larger reverse micelles (d=4nm, d=6nm), we noted that the water local density near the COM of the water pool reached bulk water density, which indicates the presence of both a central bulk-like phase and an interfacial phase in these two larger reverse micelles. However, the density of water decreased quite rapidly with increasing distance from the COM. In the case of the two smaller reverse micelles (d=1nm, d=2nm), the central density did not reach bulk water density.

Accordingly, the absence or incompleteness of a bulk region in a smaller micellar water pool may lead to structural and dynamic differences of the water molecules, which could impact the behavior of excess proton.

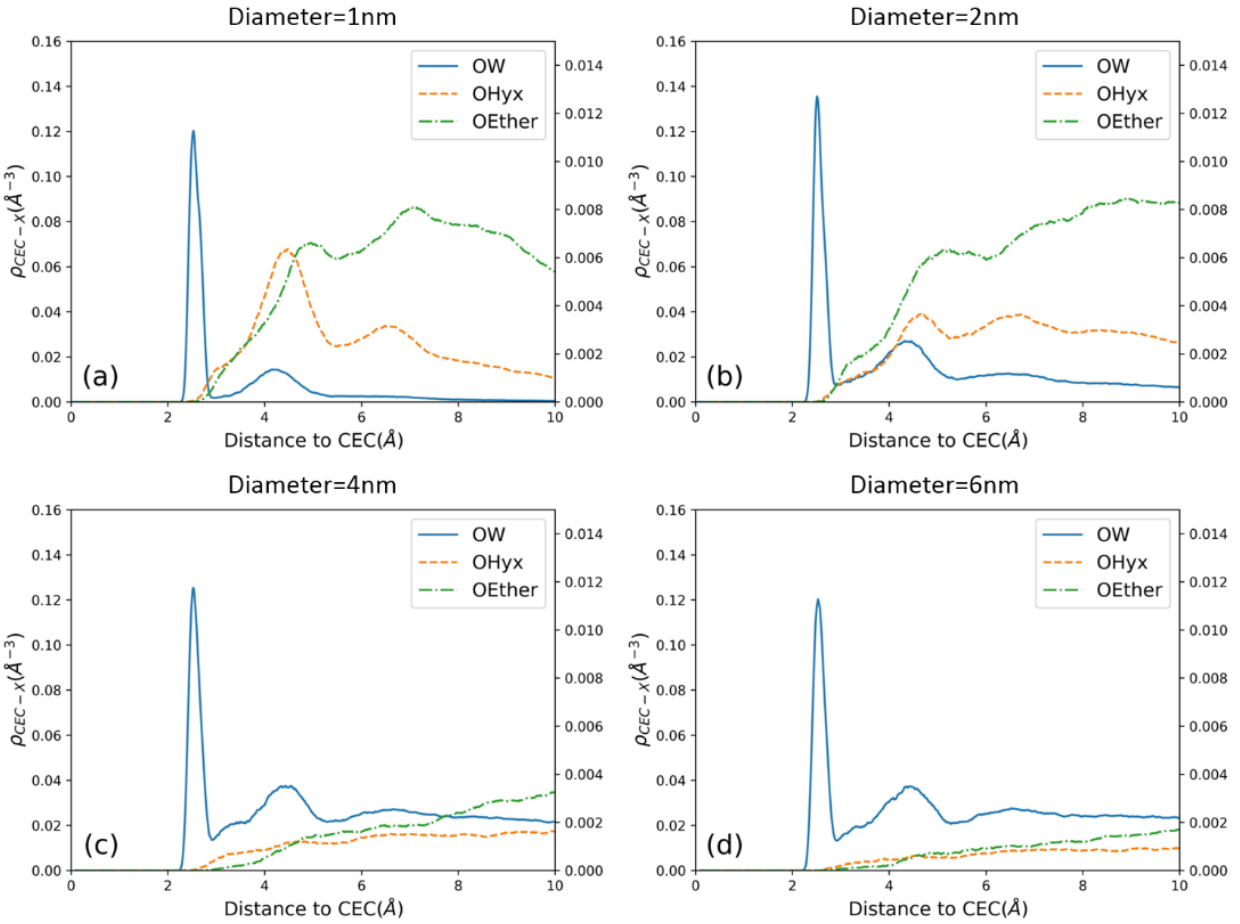

Figure 3.3 Local density profiles with pivot oxygen (O*) as center of different micellar sizes: (a) diameter=1nm, (b) d=2nm, (c) d=4nm and (d) d=6nm. OW: oxygen atom water molecule, OHyx: hydroxyl oxygen in surfactant head group, OEther: ether oxygen in surfactant head group

3.3.2 Micellar Solvation of Hydrated Excess Protons

The hydrated excess proton is usually described as two limiting structures: a Zundel cation, $H_5O_2^+$, and the Eigen cation, $H_9O_4^+$. In bulk water, it has been proposed that the excess proton

migrates through the hydrogen bond network from one water molecule to another, in an Eigen-Zundel-Eigen sequence. In confined systems such as reverse micelles, it is important to recognize the underlying impact of inhomogeneity, as well as the interfacial effect on the PT process. The relatively low water density near the interface is highly likely to impact the hydrogen bond network in the interfacial region, which in turn affects the PT process. In MS-RMD, the location of the excess protonic center of excess charge (CEC) can be defined by:

$$\boldsymbol{r}_{CEC} = \sum_{i=1}^{N} c_i^2 \, \boldsymbol{r}_{COC}^i \tag{3.2}$$

in which $\boldsymbol{r}_{COC}^i$ is the center of charge of the hydronium cation in the *i*-th MS-RMD basis eigenstate. The eigenstate with the largest c_i is known as the "pivot" state, and the hydronium oxygen in such a state is known as the pivot oxygen (hereafter referred to O*). Figure 3.3 shows a density profile depicting the solvation structure of the hydrated excess proton cation with O* as the reference point. In all four reverse micelle systems, the OW plots present two peaks, representing the first and the second shell of the hydronium-like cation (the core of the hydrated excess proton structure). In Figure 3.3(a), the oxygen atoms in the surfactant head group (OHyx and OEther) contribute considerably to the formation of the second solvation shell. With increasing micellar water pool size, the contribution of the surfactant head group to the second solvation shell diminishes. Based on the data presented in Figures 3.2 and 3.3, there is a strong interaction between the hydronium-like cation core and the surfactant in the smaller reverse micelles, suggesting that the hydrated excess proton is located near the interface. As micellar size increases and the water pool becomes more bulk-like, the interaction between the hydronium and the surfactant molecules weakens.

To further verify the binding between the excess proton and the interface, we examined the probability density function (PDF) of the distance between the excess proton CEC and the COM of the water pool (see Figure 3.4). The colored lines in this figure depict the PDF, while the vertical dashed lines depict the GDS of the micellar water pool. For all four reverse micelles, the PDF peak was observed to be more distant from the COM and nearer the GDS, indicating that the center of excess charge (i.e., the hydrated excess proton) has a tendency to move away from the center of the water pool and reside near the interface, even for non-ionic surfactants. With increasing micellar size, the PDF shows a wider distribution, with the peak moving left and away from the GDS, indicating a weaker binding between the hydrated excess proton and the interface.

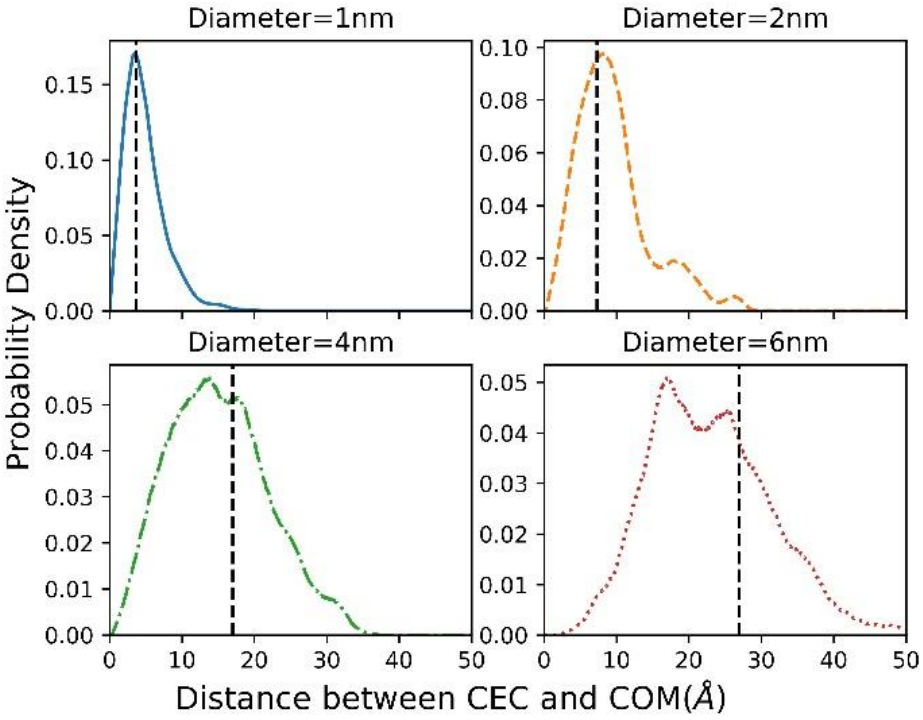

Figure 3.4 Probability density of hydrated excess proton CEC (y-axis) corresponding to the distance to COM (x-axis) in four reverse micelle systems. The dashed vertical line is the Gibbs Dividing Surface (GDS).

Furthermore, Figure 3.5 provides a 3D visualization of CEC probability density for each system during one independent simulation run of 3 ns, where each data point is a CEC coordinate relative to COM at one time step and is color-coded according to the probability density of the CEC through the entire time series. The blue dot represents the COM and the black wireframe represents the GDS. As shown in Figure 3.5, the hydrated excess proton CEC density accumulates mostly away from the COM and near the interface radially, which is consistent with results provided in Figure 3.4. The CEC also tends to be laterally trapped in a certain region of the interface, leaving much of the interfacial phase unvisited.

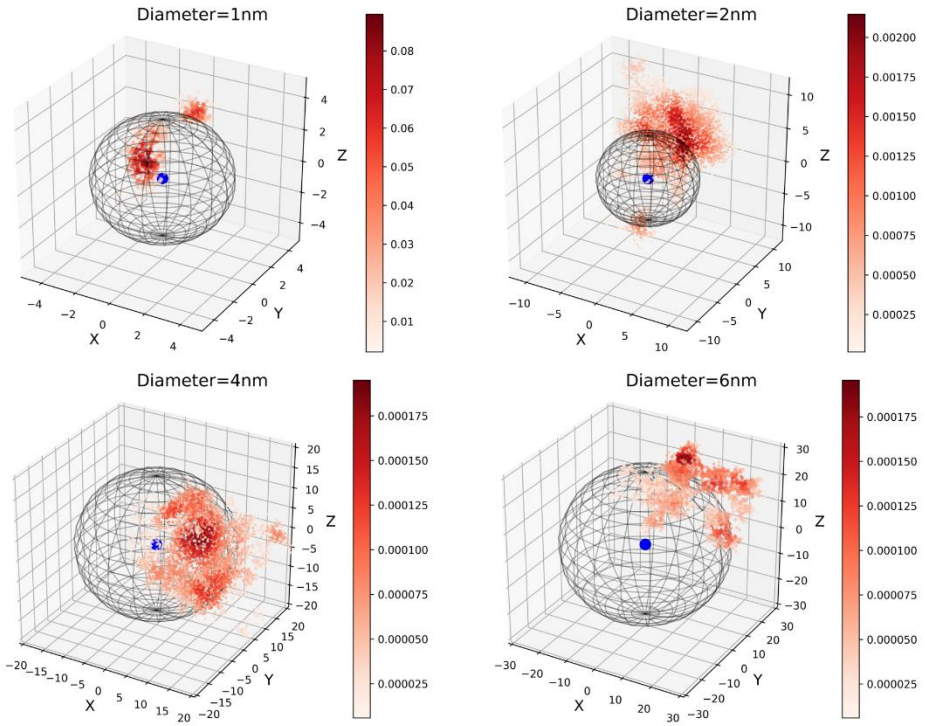

Figure 3.5 3D visualization of CEC probability density over a 3-ns time period for all four reverse micelles systems: d= 1 nm, d= 2 nm, d= 4 nm, and d=6 nm. The hydrated excess proton CEC coordinates are relative to the COM and are color-coded according to the local density of CEC across the entire time series. The blue dot denotes the origin (COM coordinate), and the black wireframe denotes the GDS.

Based on results presented in Figures 3.4 and 3.5, we conclude that the excess proton in the reverse micelles is localized near the interfacial region, both radially and laterally. Moreover, the binding between the excess proton and the interface was found to decrease with increasing micellar diameter.

3.3.3 Proton Transport in Reverse Micelles

Having established the nature of micellar solvation of the hydrated excess protons, we then examined the underlying dynamical characteristics that contribute to the PT process in the reverse micelles. First, we calculated the diffusive behavior of the hydrated excess proton and the water molecules in reverse micelle. In bulk systems, the diffusion of a species can be described with the usual Einstein relation:

$$\langle r^2 \rangle_{t\to\infty} = 6Dt \tag{3.3}$$

in which D is the diffusion coefficient and $\langle r^2 \rangle$ is the mean squared displacement (MSD) of the species, assuming the origin of all trajectories is taken to be zero. The Einstein relation describes a linear relation between the MSD and time. However, in confined systems there is often not a linear relation between the MSD and time, but instead a power law relation (see., e.g., ref[39] for the case of proton exchange membranes):

$$\langle r^2 \rangle = 6D_\alpha t^\alpha \tag{3.4}$$

where $0 < \alpha < 1$ for sub-diffusivity and D_α is a parameter with the same units as the diffusive coefficient. Figure 3.6 depicts the MSD of water oxygen and the excess proton CEC in each of the four reverse micelle systems. The parameters of sub-diffusivity (α and D_α) of water and CEC were obtained with least square fitting according to Equation (3.4) and shown in Table 3.2. The micellar

diffusion of water and excess proton shows to be slower compared to the bulk system. For our study, we observed a clear trend that with increasing water pool size, both the diffusivity of the water and hydrated excess proton CEC increased, as expected. The slowing down of the relaxation rate of water in reverse micelles has in fact been widely confirmed via various experimental approaches including pulsed NMR,[40] fluorescent spectroscopy,[41-43] dielectric measurements,[44-45] as well as by computational approaches.[46-47]

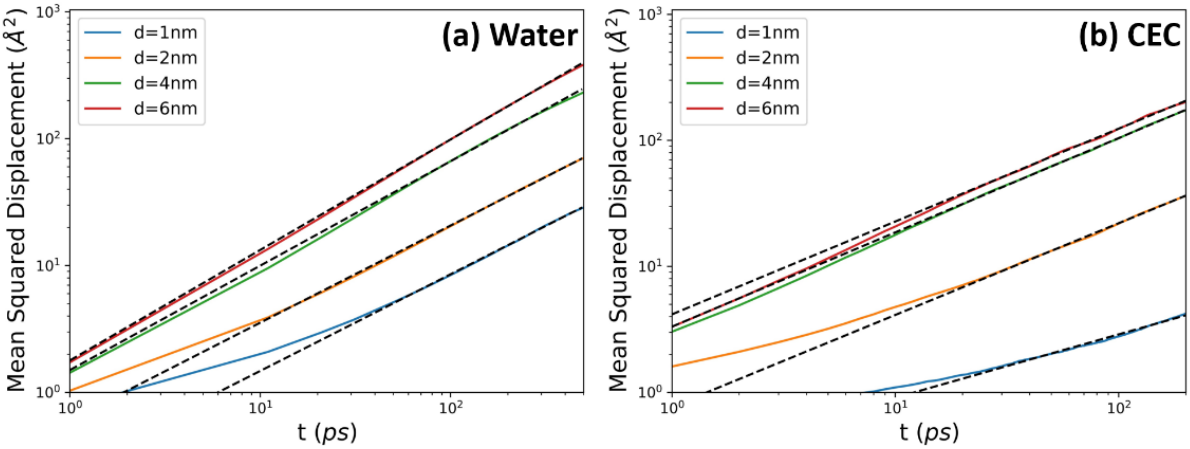

Figure 3.6 Mean squared displacement of oxygen in (a) water, and (b) hydrated excess proton CEC in four reverse micelle systems, plotted in log-log scale.

The diffusion of excess proton represents the collective outcome of the vehicular motion of hydronium cations (H_3O^+) and the Grotthuss hopping of protons from one water molecule to another; accordingly, the vehicular motion of excess proton should be strongly correlated with the water diffusion. For instance, with increasing micellar diameter and reduced effective interaction between the excess proton and the interface, the diffusion of the excess proton increases. Slow diffusion of interfacial water slows the diffusion of the excess proton once it reaches the interface and helps to trap the proton. Moreover, it has been shown that the rearrangement of the hydrogen

bond network as a whole plays a key role in long-range structural diffusion,[49-50] which in turn is correlated with water diffusion. The simultaneous slowing down of the diffusive motion of water molecules and the hydrated proton CEC is consistent with the correlation mentioned above.

Table 3.2 Fitted parameters of sub-diffusivity for water oxygen and hydrated excess proton (CEC) in each reverse micelle.

	d=1nm	d=2nm	d=4nm	d=6nm	bulk[38, 48]
α_{OW}	0.76	0.77	0.82	0.87	1.0
$D_{\alpha OW}$ ($Å^2$/ps)	0.042	0.10	0.25	0.30	0.23
α_{CEC}	0.50	0.73	0.74	0.74	1.0
$D_{\alpha CEC}$ ($Å^2$/ps)	0.047	0.13	0.55	0.69	0.43

It is also valuable to evaluate the rate of proton hopping in reverse micelles. Using the MS-RMD framework, proton hopping events can be identified by observing the identity change of the pivot hydronium in the dynamic algorithm. Specifically, two types of proton hopping can be observed: (1) oscillatory shuttling, during which the excess proton hops back and forth between the pivot hydronium cation and a water molecule in its first solvation shell; and (2) Grotthuss shuttling, during which the proton hops first and then on to a third water molecule instead of hopping back to its donor. Grotthuss shuttling should be considered as the primary contributor to the mobility of excess proton. Accordingly, we utilized a "forward hop" accumulation function to evaluate the rate of Grotthuss shuttling. The forward hop equation is given as:

$$h(t) = h(t-1) + \delta h(t)$$
$$h(0) = 0 \tag{3.5}$$

in which t is the time step, h is the accumulated hopping. The increment $\delta h(t)$ is 0 if there is no proton hop, 1 if the proton hops to a new receptor, and -1 if it hops back to the previous donor. To clarify the definition of "previous donor", we consider a scenario in which the pivot hydronium identity follows this sequence: 1-2-3-2-3. The $\delta h(t)$ for each step will be: +1, +1, -1, +1, which is based on the fact that when the proton hops from 3 back to 2, the "previous donor" of water 2 becomes water 1 again. This function distinguishes the aforementioned two shuttling events. This type of accumulation function measures the topological distance between hydronium at time 0 and at time t in terms of the number of proton hops.

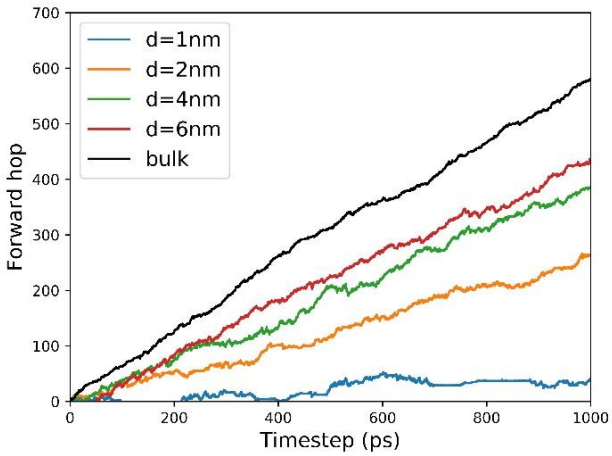

Figure 3.7 Forward excess proton hop function calculated from an MD trajectory from each reverse micelle system and a bulk water system.

Figure 3.7 depicts the forward proton hop function for each of the four reverse micelle systems and the bulk water system. In a water pool as small as 1nm in diameter, there is no bulk-

like region in the pool, and all water molecules are interfacial. Moreover, the almost flat forward hop function indicates that the interfacial environment has greatly impeded the proton hopping. With increasing micellar size, however, the proton hopping rate increases accordingly. Keeping in mind that the solvation environment of the excess proton becomes more bulk-like with increasing micellar size, Figure 3.7 provides direct evidence of the low proton hopping rate of the interfacial excess protons. Both proton transport components—the vehicular motion of the hydronium cation and Grotthuss proton hopping—clearly become slower in reverse micelle systems, as a result of the slow PT near the interface which makes it difficult for hydrated excess protons to move back to bulk-like regions once they reach the interface. This explanation for the slowed hydrated proton diffusion differs from that of Van der Loop et al.,[24] who assumed the excess proton would not be at the interface.

3.3.4 Discussion on Slow Micellar Proton Hopping

In this section, we add additional insight to the low proton hopping rate in reverse micelles. One possible factor for this behavior is the difference in structural properties of the hydronium-like complex. To define a hydronium complex, one must first locate the pivot or "core" hydronium cation. For every water molecule in its first solvation shell, δ as defined in is calculated as:

$$\delta = \left| d_{O^*H} - d_{O_WH} \right| \tag{3.6}$$

in which d_{O^*H} is the distance between the shared hydrogen atom and the hydronium oxygen, and d_{O_WH} is the distance between the shared hydrogen atom and the water oxygen. The water molecule with the minimal δ was identified as the "special pair"[51] of the hydronium cation. Between the hydronium cation and its "special pair", a Zundel-like complex could be identified.

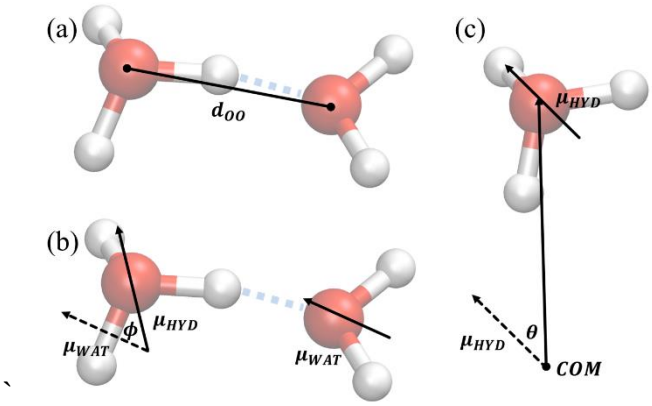

Figure 3.8 Three characteristics used to describe the structure of the hydronium-like complex. (a) $\boldsymbol{d_{OO}}$, the distance between the two oxygen atoms; (b) $\boldsymbol{\phi}$, the angle between the dipole moment of the hydronium cation and water molecule; (c) $\boldsymbol{\theta}$, the angle between the dipole moment of the hydronium cation and its relative coordinate vector to the COM of the water pool.

We then introduced two characteristics to describe the structural properties of such hydronium-like complexes: (1) d_{OO}, the distance between the two oxygen atoms, and (2) ϕ, the angle between the dipole moment of the hydronium cation (μ_{HYD}) and the dipole moment of water molecule (μ_{WAT}). Both d_{OO} and ϕ represent inherent structural properties of the hydronium complex. We also defined θ as the angle between the dipole moment of the hydronium cation and its relative coordinate vector to the COM of the water pool. The angle θ is an external property that describes the orientation relationship between the hydronium cation and the interface. A small θ means the dipole moment of the hydronium cation is pointing radially outwards from the water pool and perpendicular to the interface; therefore, a θ close to 90° indicates that the dipole moment is parallel to the interface, while a θ close to 180° indicates that it points radially inwards toward the water pool. These characteristics are illustrated in Figure 3.8.

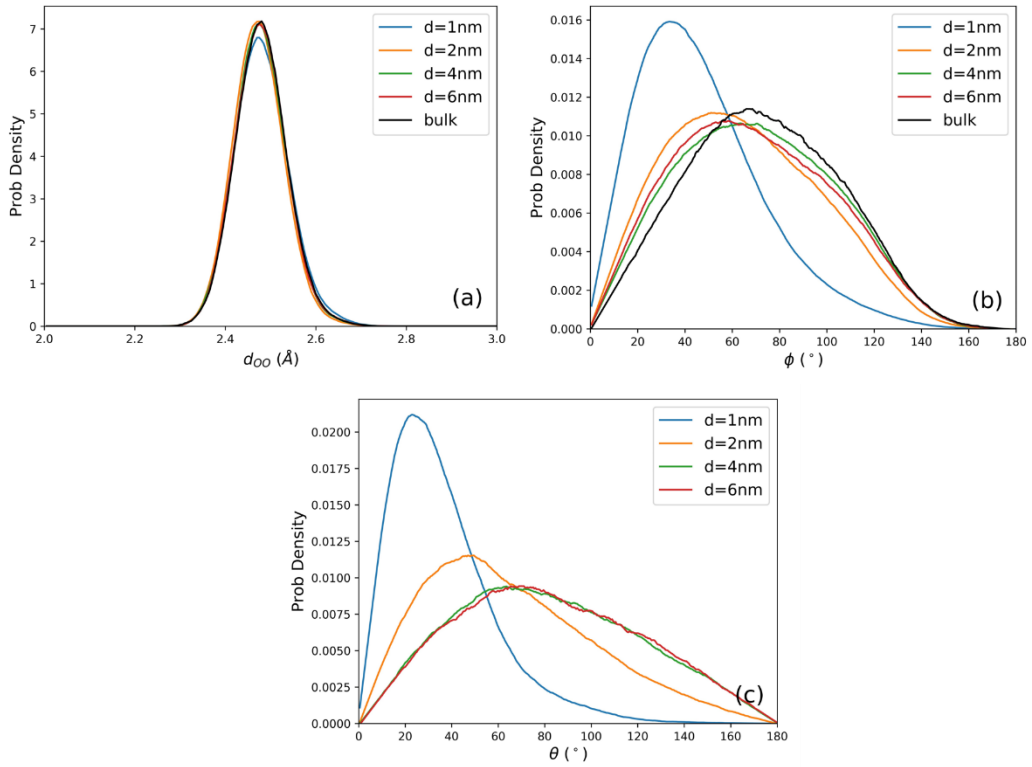

Figure 3.9 Probability density of characteristics for structural properties of hydronium-like complexes. (a) $\boldsymbol{d_{OO}}$ of reverse micelles and bulk system; (b) ϕ of reverse micelles and bulk system; (c) θ of reverse micelles.

For each reverse micelle system, the probability density distribution for every characteristic described above was calculated from the simulation trajectories. In Figure 3.9, the results from the four reverse micelle systems are depicted and compared with corresponding data from the bulk system (if applicable). First, we observed only minor differences in d_{OO} between the d=1nm micelle and the remaining systems, as shown in Figure 3.9(a). Second, a relatively larger distortion regarding the angle between two dipole moments was observed, as indicated in Figure 3.9(b). Specifically, in the d=1nm reverse micelle, the average angle between the dipole moments was significantly smaller than that of the bulk system. The structural distortion of hydronium complexes in smaller micellar water pools may be a result of low water density in the interfacial

region, as well as the participation of surfactant head groups in the solvation shells of the hydronium. It is possible that the slightly distorted structure of the hydronium complex interrupts the local hydrogen bond (HB) network near the excess proton and hinders the PT process in smaller reverse micelles. Next, as shown in Figure 3.9(c), we observed that θ is a rather distinct structural property across the four reverse micelle systems. With increasing micellar size, the mode of probability density distribution of θ increased, with the distribution widening. This finding indicates that (1) the orientation of the hydronium dipole moment evolves from radial to lateral, and (2) re-orientation becomes relatively free with increasing micellar size. It should also be noted that a locked re-arrangement of the hydronium dipole exerted a negative impact on the delocalization of the excess proton and hindered the relaxation of the hydrogen bonds nearby.

Furthermore, it is likely that low interfacial water density and the participation of non-reactive surfactant head groups in the solvation environment of the hydronium-like cation slowed down proton hopping. As discussed in an earlier section of this paper, the excess proton resides in the interfacial region of the micellar water pool where the water density is lower and is mixed with surfactant head groups. The difficulty for the hydronium cation to locate water molecules and form a complete HB network hinders the excess proton from hopping. The low interfacial water density may also contribute to the locked dipole orientation of the hydronium cation, which can be attributed to a difficulty in breaking an existing HB network to form a new one.

We next investigated the overall dynamics of the HB network of all water molecules in micellar water pools. In this report, the hydrogen bonds are identified according to specific geometric criteria: a hydrogen bond is recognized when the distance between donor oxygen and

acceptor oxygen is within 3.0 Å and the O-H-O angle is between 160° and 180°. Accordingly, we used a time correlation function[52] to evaluate the relaxation time of the hydrogen bonds:

$$C_{HB}(t) = \frac{\langle h(0) \cdot h(t) \rangle}{\langle h \rangle} \tag{3.7}$$

in which $h(t)$ is 1 if the tagged hydrogen bond exists at time t and 0 if it does not. The $\langle ... \rangle$ symbol denotes averaging over all atom pairs feasible for hydrogen bonding and over the entire simulation trajectory. This correlation function $C_{HB}(t)$ describes the probability that a certain HB remains intact after a certain amount of time t, disregarding possible HB breakage during interim times. The associated relaxation time of the $C_{HB}(t)$ function describes the structural relaxation of the hydrogen bond network. The autocorrelation of HBs in the bulk system can be fit with an exponential decay:[53]

$$C_{HB}(t) = a \exp\left(-\frac{t}{\tau}\right) \tag{3.8}$$

However, the micellar HB autocorrelation functions are clearly not exponential and can be very well fit with a bi-exponential decay such that:

$$C_{HB}(t) = a_1 \exp\left(-\frac{t}{\tau_1}\right) + a_2 \exp(-\frac{t}{\tau_2}) \tag{3.9}$$

in which $\tau_1 < \tau_2$. The bi-exponential decay behavior of hydrogen bonding in micellar water pools indicates that there was a second process proceeding simultaneously alongside the normal structural relaxation of the HB network. The results of $C_{HB}(t)$ and the fitted plots for the four reverse micelle systems and bulk water system are shown in Figure 3.10. The fitted parameters are listed in Table 3.3.

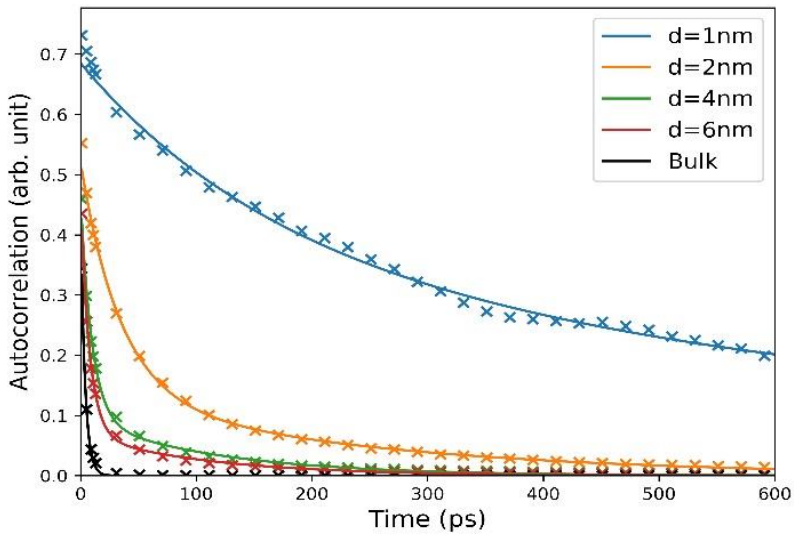

Figure 3.10 $\boldsymbol{C_{HB}(t)}$ of d=1nm, d=2nm, d=4nm and d=6nm reverse micelle systems and bulk system. Original simulation results are indicated by crosses, and fitted bi-exponential figures are depicted as solid lines.

Table 3.3 Parameters of the exponential/bi-exponential decay of $\boldsymbol{C_{HB}(t)}$ in the reverse micelles and bulk systems

	a_1	τ_1	a_2	τ_2
d=1nm	0.12	29.1	0.61	485.9
d=2nm	0.30	23.9	0.23	134.7
d=4nm	0.36	8.1	0.12	84.5
d=6nm	0.38	6.9	0.09	78.1
bulk (MS-RMD5)	0.43	3.78	-	-

We note that the τ values we obtained for the bulk system are comparable with previous results.[54] For the four reverse micelle systems investigated in this study, it should also be noted that with increasing micellar size, both τ_1 and τ_2 decreased accordingly, indicating a faster relaxation for both processes, as expected. Thus, we assume that the shorter τ_1 represents a short-range relaxation process of the HB, while the longer τ_2 correlates to the long-range micellar diffusion of HB pairs (i.e., water molecules and hydronium-like hydrated proton cations). The size effects of short-range HB relaxation can be attributed to the slow relaxation of micellar water. With increasing micellar size, the water pool becomes more bulk-like, and the rate of water relaxation intensifies. As a result, the short-range relaxation of HB also increases. Conversely, we assume that the size effect of long-range HB relaxation is a result of slow micellar water diffusion, as described in Section 3.3.2 and shown in Figure 3.6(a). Spectroscopic research efforts conducted by Fayer et al.[55-56] revealed similar size effect, relating the overall slower orientation relaxation in micellar water pools of smaller and intermediate sizes to the slow water dynamics of the interfacial water shell. In short, immobilized micellar interfacial water[40-47] slows the relaxation of hydrogen bonding, thus promoting its greater stability after a certain amount of time.

3.4 Conclusions

Non-ionic aqueous reverse micelles are valuable for studying confined aqueous systems. In this work, we performed MS-RMD simulations of one hydrated excess proton in non-ionic reverse micelles of four varying sizes, with the goal of determining the general impact on the behavior of the excess proton posed by the confinement in these micelles. Our simulations present a microscopic analysis of micellar water pool behavior consistent with prior research efforts.[19-22] In our reverse micelles, the hydrated excess proton remains near the interface and also interacts

with surfactant head groups, which participates in the formation of a second solvation shell. The hydrated excess proton is found to be localized both radially and laterally near the interface.

This investigation also confirmed that proton transport is slow in reverse micelles, which we ascribe to both the slow vehicular motion of hydronium-like cations and a lower proton Grotthuss hopping rate. The former tendency is also connected to the slow diffusion of interfacial water, which is consistent with previous theoretical[46-47] and experimental[40-45] findings. To further elucidate the impact of the low proton hopping rate, we analyzed the structure of the hydronium-like complex. The resulting data confirmed that slow proton hopping occurs as a result of both the enhanced interfacial solvation of the excess hydrated proton and the immobilization of the interfacial water. Low water density in the interfacial region (i.e., where the hydrated excess proton resides) makes it difficult for an excess proton to form a complete HB network around it, thus hindering the proton hopping. Moreover, the orientation of the hydronium is locked because of the difficulty in rearranging the existing HB network and forming a new one. For the overall HB network, we observed a bi-exponential decay of the micellar HB autocorrelation function involving (a) short-range HB relaxation, and (b) long-range micellar solvation of HB pairs. The two relaxation times, τ_1 and τ_2, both showed a monotonic decreasing trend with increasing micellar size. In particular, we can attribute micellar water relaxation to the short-range τ_1, and micellar HB pair diffusion to the long-range τ_2. With increasing micellar size, the hydrated excess proton more easily leaves from the interface and the surrounding solvation environment becomes less interface-like and more bulk-like, thus decreasing the relaxation time for both processes.

In the future, it will be interesting to explore how other surfactants could impact confinement effects on proton transport. For instance, Rosenfeld and Schmuttenmaer[57] reported

that the properties of a given surfactant will impact the hydrogen bond network among water molecules, which in turn may influence the PT process. Another potentially interesting direction for a future study would be to construct a set of reverse micelles with increasing diameter, such that the behavior of excess proton may eventually conforms to proton behavior in the bulk system. The downside of such an investigation is that it can be expensive and time-consuming to conduct all-atom molecular dynamics simulation on such large systems because of the large number of atoms in surfactants and solvent molecules. One possible way to overcome this hurdle is to construct coarse-grained (CG) reverse micelle systems using a recently developed "Ultra-CG" method in which the CG interactions are dependent on the local environment via "states" inside the CG sitesa.[58] As can be seen from a recent study examining their performance in complex interfacial systems,[59] this Ultra-CG approach is expected to distinguish the different environments of micelle molecules and provide significantly more accurate structural correlations.

3.5 References

1. Roy, A.; Hickner, M. A.; Lee, H.-S.; Badami, A.; Yu, X.; Li, Y.; Glass, T.; McGrath, J. E., Transport Properties of Proton Exchange Membranes. *ECS Transactions* **2007**, *2*, 45-54.

2. Petersen, M. K.; Hatt, A. J.; Voth, G. A., Orientational Dynamics of Water in the Nafion Polymer Electrolyte Membrane and Its Relationship to Proton Transport. *The Journal of Physical Chemistry B* **2008**, *112*, 7754-7761.

3. Jorn, R.; Voth, G. A., Mesoscale Simulation of Proton Transport in Proton Exchange Membranes. *Journal of Physical Chemistry C* **2012**, *116*, 10476-10489.

4. Arntsen, C.; Savage, J.; Tse, Y. L. S.; Voth, G. A., Simulation of Proton Transport in Proton Exchange Membranes with Reactive Molecular Dynamics. 2016; Vol. 16, pp 695-703.

5. Savage, J.; Voth, G. A., Proton Solvation and Transport in Realistic Proton Exchange Membrane Morphologies. *Journal of Physical Chemistry C* **2016**, *120*, 3176-3186.

6. Rao, Z.; Zheng, C.; Geng, F., Proton Conduction of Fuel Cell Polymer Membranes: Molecular Dynamics Simulation. *Computational Materials Science* **2018**, *142*, 122-128.

7. Popović, D. M.; Stuchebrukhov, A. A., Electrostatic Study of the Proton Pumping Mechanism in Bovine Heart Cytochrome <I>C</I> Oxidase. *Journal of the American Chemical Society* **2004**, *126*, 1858-1871.

8. Siegbahn, P. E. M.; Blomberg, M. R. A., Proton Pumping Mechanism in Cytochrome C Oxidase. *Journal of Physical Chemistry A* **2008**, *112*, 12772-12780.

9. Lee, S.; Swanson, J. M. J.; Voth, G. A., Multiscale Simulations Reveal Key Aspects of the Proton Transport Mechanism in the Clc-Ec1 Antiporter. *Biophysical Journal* **2016**, *110*, 1334-1345.

10. Liang, R.; Swanson, J. M. J.; Wikström, M.; Voth, G. A., Understanding the Essential Proton-Pumping Kinetic Gates and Decoupling Mutations in Cytochrome <I>C</I> Oxidase. *Proceedings of the National Academy of Sciences* **2017**, *114*, 5924-5929.

11. Mayes, H. B.; Lee, S.; White, A. D.; Voth, G. A.; Swanson, J. M. J., Multiscale Kinetic Modeling Reveals an Ensemble of Cl-/H+Exchange Pathways in Clc-Ec1 Antiporter. *Journal of the American Chemical Society* **2018**, *140*, 1793-1804.

12. Petersen, M. K.; Iyengar, S. S.; Day, T. J. F.; Voth, G. A., The Hydrated Proton at the Water Liquid/Vapor Interface. *Journal of Physical Chemistry B* **2004**, *108*, 14804-14806.

13. Iuchi, S.; Chen, H.; Paesani, F.; Voth, G. A., Hydrated Excess Proton at Water-Hydrophobic Interfaces. *Journal of Physical Chemistry B* **2009**, *113*, 4017-4030.

14. Chen, H.; Xu, J.; Voth, G. A., Unusual Hydrophobic Interactions in Acidic Aqueous Solutions. *The Journal of Physical Chemistry B* **2009**, *113*, 7291-7297.

15. Yamashita, T.; Voth, G. A., Properties of Hydrated Excess Protons near Phospholipid Bilayers. *Journal of Physical Chemistry B* **2010**, *114*, 592-603.

16. Savage, J.; Tse, Y.-L. S.; Voth, G. A., Proton Transport Mechanism of Perfluorosulfonic Acid Membranes. *The Journal of Physical Chemistry C* **2014**, *118*, 17436-17445.

17. Wolf, M. G.; Grubmüller, H.; Groenhof, G., Anomalous Surface Diffusion of Protons on Lipid Membranes. *Biophysical Journal* **2014**, *107*, 76-87.

18. Zhang, C.; Knyazev, D. G.; Vereshaga, Y. A.; Ippoliti, E.; Nguyen, T. H.; Carloni, P.; Pohl, P., Water at Hydrophobic Interfaces Delays Proton Surface-to-Bulk Transfer and Provides a Pathway for Lateral Proton Diffusion. *Proceedings of the National Academy of Sciences* **2012**, *109*, 9744-9749.

19. D'Aprano, A.; Lizzio, A.; Turco Liveri, V.; Aliotta, F.; Vasi, C.; Migliardo, P., Aggregation States of Water in Reversed Aot Micelles: Raman Evidence. *Journal of Physical Chemistry* **1988**, *92*, 4436-4439.

20. Jain, T. K.; Varshney, M.; Maitra, A., Structural Studies of Aerosol Ot Reverse Micellar Aggregates by Ft-Ir Spectroscopy. *Journal of Physical Chemistry* **1989**, *93*, 7409-7416.

21. Hauser, H.; Haering, G.; Pande, A.; Luisi, P. L., Interaction of Water with Sodium Bis(2-Ethyl-1-Hexyl) Sulfosuccinate in Reversed Micelles. *Journal of Physical Chemistry* **1989**, *93*, 7869-7876.

22. Belletête, M.; Lachapelle, M.; Durocher, G., Polarity of Aot Micellar Interfaces: Use of the Preferential Solvation Concepts in the Evaluation of the Effective Dielectric Constants. *Journal of Physical Chemistry* **1990**, *94*, 5337-5341.

23. De, T. K.; Maitra, A., Solution Behaviour of Aerosol Ot in Non-Polar Solvents. *Advances in Colloid and Interface Science* **1995**, *59*, 95-193.

24. Van der Loop, T. H.; Ottosson, N.; Vad, T.; Sager, W. F. C.; Bakker, H. J.; Woutersen, S., Communication: Slow Proton-Charge Diffusion in Nanoconfined Water. *Journal of Chemical Physics* **2017**, *146*, 131101.

25. Pomata, M. H. H.; Laria, D.; Skaf, M. S.; Elola, M. D., Molecular Dynamics Simulations of Aot-Water/Formamide Reverse Micelles: Structural and Dynamical Properties. *Journal of Chemical Physics* **2008**, *129*, 244503.

26. Rodriguez, J.; Martí, J.; Guàrdia, E.; Laria, D., Protons in Non-Ionic Aqueous Reverse Micelles. *Journal of Physical Chemistry B* **2007**, *111*, 4432-4439.

27. Rodriguez, J.; Laria, D.; Guàrdia, E.; Martí, J., Dynamics of Water Nanodroplets and Aqueous Protons in Non-Ionic Reverse Micelles. *Physical Chemistry Chemical Physics* **2009**, *11*, 1484-1490.

28. Fillingim, T. G.; Luo, N.; Lee, J.; Robinson, G. W., Fast and Slow Dynamic Probes in Solvent Structural Investigations. *Journal of Physical Chemistry* **1990**, *94*, 6368-6371.

29. Guss, L. S.; Kolthoff, I. M., The Distribution of Protons between Water and Other Solvents. *Journal of the American Chemical Society* **1940**, *62*, 1494-1496.

30. Petersen, M. K.; Voth, G. A., Amphiphilic Character of the Hydrated Proton in Methanol-Water Solutions. *Journal of Physical Chemistry B* **2006**, *110*, 7085-7089.

31. Martinez, L.; Andrade, R.; Birgin, E. G.; Martínez, J. M., Packmol: A Package for Building Initial Configurations for Molecular Dynamics Simulations. *Journal of Computational Chemistry* **2009**, *30*, 2157-2164.

32. Wang, J.; Wang, W.; Kollman, P. A.; Case, D. A., Automatic Atom Type and Bond Type Perception in Molecular Mechanical Calculations. *Journal of Molecular Graphics and Modelling* **2006**, *25*, 247-260.

33. Bayly, C. I.; Cieplak, P.; Cornell, W. D.; Kollman, P. A., A Well-Behaved Electrostatic Potential Based Method Using Charge Restraints for Deriving Atomic Charges: The Resp Model. *Journal of Physical Chemistry* **1993**, *97*, 10269-10280.

34. Dupradeau, F. Y.; Pigache, A.; Zaffran, T.; Savineau, C.; Lelong, R.; Grivel, N.; Lelong, D.; Rosanski, W.; Cieplak, P., The R.E.D. Tools: Advances in Resp and Esp Charge Derivation and Force Field Library Building. *Physical Chemistry Chemical Physics* **2010**, *12*, 7821-7839.

35. M. J. Frisch, G., et al., Gaussian 09, Revision D.01. *Gaussian 09, Revision D.01* **2009**, *1*, 1.

36. Vanquelef, E.; Simon, S.; Marquant, G.; Garcia, E.; Klimerak, G.; Delepine, J. C.; Cieplak, P.; Dupradeau, F. Y., R.E.D. Server: A Web Service for Deriving Resp and Esp Charges and Building Force Field Libraries for New Molecules and Molecular Fragments. *Nucleic Acids Research* **2011**, *39*, W511-W517.

37. Plimpton, S.; Crozier, P.; Thompson, A., Lammps-Large-Scale Atomic/Molecular Massively Parallel Simulator. . *Sandia National Laboratories* **2007**, *18*, 43.

38. Park, K.; Lin, W.; Paesani, F., A Refined Ms-Evb Model for Proton Transport in Aqueous Environments. *Journal of Physical Chemistry B* **2012**, *116*, 343-352.

39. Savage, J.; Voth, G. A., Persistent Subdiffusive Proton Transport in Perfluorosulfonic Acid Membranes. *Journal of Physical Chemistry Letters* **2014**, *5*, 3037-3042.

40. Urry, D. W.; Peng, S.; Xu, J.; McPherson, D. T., Characterization of Waters of Hydrophobic Hydration by Microwave Dielectric Relaxation. *Journal of the American Chemical Society* **1997**, *119*, 1161-1162.

41. Levinger, N. E., Ultrafast Dynamics in Reverse Micelles, Microemulsions, and Vesicles. *Current Opinion in Colloid and Interface Science* **2000**, *5*, 118-124.

42. Riter, R. E.; Willard, D. M.; Levinger, N. E., Water Immobilization at Surfactant Interfaces in Reverse Micelles. *The Journal of Physical Chemistry B* **1998**, *102*, 2705-2714.

43. Zhang, J.; Bright, F. V., Nanosecond Reorganization of Water within the Interior of Reversed Micelles Revealed by Frequency-Domain Fluorescence Spectroscopy. *Journal of Physical Chemistry* **1991**, *95*, 7900-7907.

44. Fukuzaki, M.; Miura, N.; Shinyashiki, N.; Kurita, D.; Shioya, S.; Haida, M.; Mashimo, S., Comparison of Water Relaxation Time in Serum Albumin Solution Using Nuclear Magnetic Resonance and Time Domain Reflectometry. *Journal of Physical Chemistry* **1995**, *99*, 431-435.

45. Grant, E. H.; McClean, V. E. R.; Nightingale, N. R. V.; Sheppard, R. J.; Chapman, M. J., Dielectric Behavior of Water in Biological Solutions: Studies on Myoglobin, Human Low-Density Lipoprotein, and Polyvinylpyrrolidone. *Bioelectromagnetics* **1986**, *7*, 151-162.

46. Mashl, R. J.; Joseph, S.; Aluru, N. R.; Jakobsson, E., Anomalously Immobilized Water: A New Water Phase Induced by Confinement in Nanotubes. *Nano Letters* **2003**, *3*, 589-592.

47. Senapati, S.; Berkowitz, M. L., Water Structure and Dynamics in Phosphate Fluorosurfactant Based Reverse Micelle: A Computer Simulation Study. *Journal of Chemical Physics* **2003**, *118*, 1937-1944.

48. Arntsen, C.; Chen, C.; Voth, G. A., Reactive Molecular Dynamics Models from Ab Initio Molecular Dynamics Data Using Relative Entropy Minimization. *Chemical Physics Letters* **2017**, *683*, 573-578.

49. Berkelbach, T. C.; Lee, H. S.; Tuckerman, M. E., Concerted Hydrogen-Bond Dynamics in the Transport Mechanism of the Hydrated Proton: A First-Principles Molecular Dynamics Study. *Physical Review Letters* **2009**, *103*, 238302.

50. Lapid, H.; Agmon, N.; Petersen, M. K.; Voth, G. A., A Bond-Order Analysis of the Mechanism for Hydrated Proton Mobility in Liquid Water. *Journal of Chemical Physics* **2005**, *122*, 014506.

51. Markovitch, O.; Chen, H.; Izvekov, S.; Paesani, F.; Voth, G. A.; Agmon, N., Special Pair Dance and Partner Selection: Elementary Steps in Proton Transport in Liquid Water. *Journal of Physical Chemistry B* **2008**, *112*, 9456-9466.

52. Luzar, A.; Chandler, D., Hydrogen-Bond Kinetics in Liquid Water. *Nature* **1996**, *379*, 55.

53. Chandra, A., Effects of Ion Atmosphere on Hydrogen-Bond Dynamics in Aqueous Electrolyte Solutions. *Physical Review Letters* **2000**, *85*, 768.

54. Xu, H.; Stern, H. A.; Berne, B. J., Can Water Polarizability Be Ignored in Hydrogen Bond Kinetics? *Journal of Physical Chemistry B* **2002**, *106*, 2054-2060.

55. Moilanen, D. E.; Fenn, E. E.; Wong, D.; Fayer, M. D., Water Dynamics in Large and Small Reverse Micelles: From Two Ensembles to Collective Behavior. *The Journal of chemical physics* **2009**, *131*, 014704.

56. Fayer, M. D., Dynamics of Water Interacting with Interfaces, Molecules, and Ions. *Accounts of chemical research* **2011**, *45*, 3-14.

57. Rosenfeld, D. E.; Schmuttenmaer, C. A., Dynamics of the Water Hydrogen Bond Network at Ionic, Nonionic, and Hydrophobic Interfaces in Nanopores and Reverse Micelles. *Journal of Physical Chemistry B* **2011**, *115*, 1021-1031.

58. Dama, J. F.; Jin, J.; Voth, G. A., The Theory of Ultra-Coarse-Graining. 3. Coarse-Grained Sites with Rapid Local Equilibrium of Internal States. *Journal of Chemical Theory and Computation* **2017**, *13*, 1010-1022.

59. Jin, J.; Voth, G. A., Ultra-Coarse-Grained Models Allow for an Accurate and Transferable Treatment of Interfacial Systems. *Journal of Chemical Theory and Computation* **2018**, *14*, 2180-2197.

CHAPTER 4

PROTONATED WATER CLUSTERS IN ACETONITRILE

4.1 Introduction

In comparison to Zundel or Eigen cations, which serve as limiting solvation structures, the hydrated excess proton forms more complex solvation configurations in actuality. For example, in their investigation of proton transport in liquid water in the 1990s, Tuckerman et al.[1-2] implemented *ab initio* molecular dynamics (AIMD) simulations to investigate the process of proton transport in liquid water, confirming the presence of a "special pair" (SP) between the hydronium and nearby water molecules. Later, researchers applied MD (molecular dynamics) simulations to confirm that the three-fold symmetry of the Eigen cation is broken due to the distortion introduced by the special pair, thus forming a "distorted Eigen cation." Also, the SP was found to switch among the three water molecules in the first solvation shell on a timescale of tens of femtoseconds.[3-5] This process, which is known as the "special pair dance," suggests that the primary solvation structure of excess proton in water is a distorted Eigen cation, in which the central hydronium constantly breaks and forms SPs with one of the three water molecules within its first solvation shell.

In recent years, experimentalists have employed non-linear spectroscopy to enhance our understanding of the behavior of hydrated excess protons.[6-11] For example, Elsaesser et al.[7-8] applied ultrafast 2-dimensional infrared (2D-IR) spectroscopy to study acid-water and acetonitrile-acid-water mixtures, concluding that the Zundel motif is the predominant solvation motif of excess proton in water. In particular, in their earlier work in 2017[8], Elsaesser et al. prepared a acetonitrile-acid-water mixture with stoichiometric control (at a proton-water ratio of 1:3.5), suggesting it as a Zundel cation solution whose spectroscopic data could be used for comparison against bulk acid

solutions. More recently, it was amended that in acetonitrile, the predominant Zundel cation ($H_5O_2^+$) strongly interacts with a close-by water molecule and forms a trimer unit ($H_7O_3^+$), while preserving the Zundel cation without persistent proton localization.[7] However, considering that the dipole moment of acetonitrile is much larger than water (3.4 D vs 1.8 D),[12] the protonated water clusters in acetonitrile occupy a significantly different solvation environment in comparison to bulk water. Furthermore, minimizing the free energy of a system usually means maximizing the entropy, which implies potential existence of more than one type of protonated clusters. It is important to examine the validity using an acetonitrile-acid-water system as a benchmark system of a "Zundel cation solution."

In this study, we investigate the structures, dynamics, and thermodynamics of protonated water clusters solvated in acetonitrile. This paper is organized as follows: Section 4.2 provides a detailed description of the simulation methods we employed. Section 4.3 presents the results of the free energy calculations on different solvation species, the data findings for selected structures using Quantum Theory of Atoms in Molecules (QTAIM) analysis, as well as the topological and dynamical properties of selected species in acetonitrile. Final remarks regarding the analysis of the solvation structures and dynamics of hydrated excess proton in acetonitrile are presented in Section 4.4.

4.2 Methodology

Three different simulation methods were employed in our study: DFT-based AIMD, QTAIM, and the Multistate Empirical Valence Bond (MS-EVB) method.[13-17] The following sections describe the simulation setups and the methodological approaches adopted for data collection.

4.2.1 AIMD Umbrella Sampling Simulations

Taking into account the complexity of the system and the constant change of bonding topology in protonated water clusters, DFT-based AIMD was employed to describe acetonitrile-acid-water systems. In order to determine the structural configuration and the size of protonated water clusters in acetonitrile, the umbrella sampling method was employed to facilitate the change in cluster sizes (i.e., the number of water molecules in each cluster) and an ergodic sampling of cluster species.

The initial configuration of the simulation box, comprised of 1 hydronium cation (H_3O^+), 3 water molecules, 1 iodine anion and 95 acetonitrile molecules, periodic in all directions, was generated by the PACKMOL program.[18] The system was then equilibrated in an NPT ensemble (P=1.0 atm and T=298 K) with classical MD simulations for 5 ns using the LAMMPS[19] software package. The equilibrated configuration was then used as the initial configuration for subsequent AIMD umbrella sampling simulations. The coordination number of all water/hydronium oxygen atoms, adopted as the collective variable (CV) for the umbrella sampling, is define as:

$$C = \sum_{i,j \in O} \frac{1 - \left(\frac{r_{ij} - d_0}{r_0}\right)^6}{1 - \left(\frac{r_{ij} - d_0}{r_0}\right)^{12}} \tag{4.1}$$

where d_0 and r_0 were set at 2.5 Å and 3.0 Å, respectively. In a system of 4 water/hydronium oxygen atoms, the CV has a lower limit of 0.0 (water molecules scattering into monomers) and an upper limit of 6.0 (water molecules aggregating into a tetramer). Based on this range, 25 evenly spaced windows (0.25 coordination number units apart) were set up between CV values of 0.0 and 6.0. The force constant of the restraining potential was 5.0 kcal/mol/Å^2. The DFT-based AIMD

simulations were then performed on each of the windows. The BLYP exchange-correlation functional[20-21] was employed with Goedecker-Teter-Hutter (GTH) pseudopotentials[22] and a TZV2P basis set. In order to account for the dispersion corrections, both the original D3 Grimme dispersion interaction[23] with "zero-damping" (henceforth referred to as D3(0)) and D3 with Becke–Johnson damping (D3BJ)[24] were used in separate simulations. For the D3BJ simulations, a total of 360 ps of production trajectories was acquired180 ps of production trajectories was obtained with D3(0). All AIMD simulations were carried out with the Quickstep module in CP2K[25] and using the PLUMED enhanced sampling package.[26-27]

4.2.2 QTAIM Analysis

To analyze hydrogen bond (HB) strength in the protonated water clusters, snapshots of four cluster configurations (provided in Section 3) were extracted from the production trajectories. Cluster geometries were optimized with the BLYP-D3BJ/def2-TZVPP level of theory using the Gaussian 16 program package.[24, 28-32] For comparison with other levels of theory, structures were also optimized using "zero-damped" BLYP-D3(0) and the range-separated hybrid CAM-B3LYP-D3BJ functional, both with the def2-TZVPP basis set.[29, 33-37] Relative zero-point corrected energies were compared with CCSD(T)/def2-TZVPP single-point calculations performed on MP2/def2-TZVPP optimized structures, with the MP2 frequencies used for the zero-point corrections (denoted as CCSD(T)//MP2).[38-42] All structures were verified to be local minima by frequency calculations and thermochemical properties were obtained within the rigid rotor ⁄ harmonic oscillator approximation. HBs in each level of theory were quantified using the categorization of critical points in the electron density known as the Quantum Theory of Atoms in Molecules (QTAIM), as implemented in the Multiwfn computational chemistry package.[43]

A recent study on the analysis of the strengths of the hydrogen bonds in protonated tetrapeptides corroborates the following procedure for QTAIM assessment of HBs.[44] First, the Poincaré–Hopf theorem holds for each QTAIM critical point map, fulfilling a necessary condition for all critical points to be found. The presence of HBs was confirmed via three criteria: the bond path, the density at the bond critical point (bcp, the second order saddle point in electron density along the hydrogen bond), and the Laplacian of the density at the bcp. Only bond paths connecting hydrogen to nitrogen or oxygen were considered to be HBs. Furthermore, only bond paths with bcp charge densities within a window of 0.002–0.034 a.u., and bcp Laplacians within a window of 0.024–0.139 a.u., were considered as HBs, in accordance with parameters defined by Koch and Popelier.[45] Lastly, the ceilings on the two numerical parameters were removed when considering interactions with the solvated proton, due to the increased strength and covalent-like characteristics of its interactions in comparison to those of traditional HBs. In practice, all intermolecular bond paths connecting hydrogens to heavy atoms passed the two numerical tests and were considered as HBs. To determine the relative strengths of HBs, the potential energy density, V(r), at the bcp was used. While the experimental electron densities suggest a possible correlation between HB energies and the value of V(r),[46] the gross values of V(r) value at each bcp is reported to avoid any possible system-dependent effects within the aforementioned conversion.

4.2.3 MS-EVB Umbrella Sampling Simulations

To provide a supplementary dataset, MS-EVB umbrella sampling simulations were performed using the same simulation system and methodologies described in Section 4.2.1. The MS-EVB method was developed to account for changes in bonding topology during proton transport, without incurring the full computational cost of AIMD simulations. Within the MS-EVB

framework, the state of the system is described as a linear combination of "basis states," $|i\rangle$, each of which delineates a possible bonding topology of the system. The basis states are then coupled with each other via off-diagonal elements in a Hamiltonian-like matrix and the ground-state eigenvector is calculated on-the-fly during the simulation. The ground-state eigenvector facilitates a realistic description of the hydration structure of the excess proton and yields the population of each basis state population, which are then adopted for the calculation of atomistic forces through Hellman-Feynman theorem. A detailed description of the MS-EVB framework can be found in the literature.[47-48]

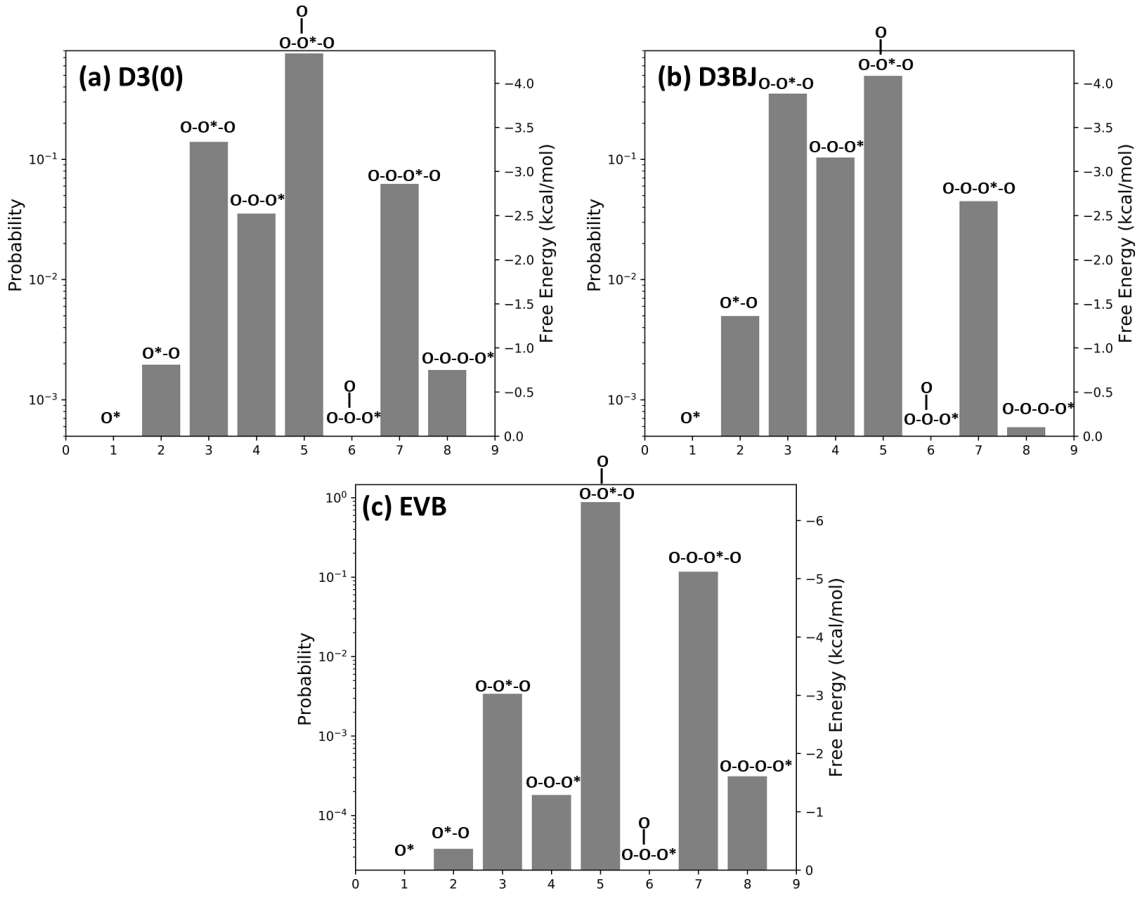

Figure 4.1 Free energy profiles of protonated water cluster species calculated from (a) BLYP+D3(0) AIMD trajectories, (b) BLYP+D3BJ AIMD trajectories, and (c) MS-EVB 3.2 trajectories. The species, in the order of the x-axis of the figures, are 1) naked hydronium, 2)

classical Zundel cation, 3) $H_7O_3^+$ with excess charge located in middle, 4) $H_7O_3^+$ with excess charge at the edge, 5) classical Eigen cation, 6) Eigen cation with excess charge at the edge, 7) four-water chain with excess charge in middle, and 8) four-water chain with excess charge at the edge.

The present study employs the MS-EVB 3.2 model, the details and parameters of which can be found in a prior publication.[17] For the present MS-EVB simulations of the protonated water clusters in acetonitrile, the simulation box was kept identical to the one described in Section 4.2.1. The simulations were carried out with a modified version[49-50] of the LAMMPS MD software,[19] and long-range electrostatic interactions were calculated using the particle-particle-particle-mesh (PPPM) method with the relative error set to 10^{-6}. All simulations were conducted in a constant NVE ensemble. For each window, a total of 5 ns of production trajectories was acquired.

4.3 Results and Discussions

4.3.1 Free Energy Profiles of Protonated Water Cluster Species

Eight possible protonated water cluster species were identified based on the size (number of molecules) in the cluster and the location of the pivot oxygen, which is defined as the oxygen atom most closely bound to three surrounding hydrogen atoms. The free energy profiles for these species are shown in Figure 4.1. Note that the free energies given by D3(0) and D3BJ trajectories are qualitatively consistent, indicating that the primary solvation species (the one with highest probability and lowest free energy) is Species 5, an $H_9O_4^+$ cluster with the pivot oxygen in the center, i.e., an Eigen cation. The second most predominant species is $H_7O_3^+$ with the charge localized in the middle of the three water molecules (Species 3). The free-energy difference between Species 3 and its variant Species 4 was found to be about 1 kcal/mol, indicating that the excess charge is more likely to localize in the middle than on one of the terminal water molecules.

If Species 3 were indeed a Zundel cation that interacts closely with an additional water molecule, the excess proton should be found on the central and the terminal water molecules with equal likelihood due to the delocalization of the excess charge. Therefore, the populations in Specie 3 and 4 should become indistinguishable. However, this outcome was not found to be the case. Other solvation species, e.g., four-water chains (Species 7) and naked Zundel cations (Species 2), were also found to be present with lower probabilities. A visual inspection of the trajectories indicated that the extra water molecules absent in the protonated water clusters were biased away by the applied umbrella potentials, as intended.

The free energy profile calculated from MS-EVB trajectories shows generally consistent results compared to AIMD simulations, albeit favoring four-water chains (Specie 7 and 8) over three-water clusters, possibly due to the inability of explicit charge transfer to acetonitrile in the current EVB model.[17]

4.3.2 QTAIM Analysis on Selected Structures

4.3.2.1 Benchmarks of Different Levels of Quantum Mechanics Methods

We first benchmark different levels of quantum mechanics for the water + acetonitrile system. Two structures (as shown in Figure 4.2), one straight-on hydrogen bonding (A), another with two weak contacts (B), were tested using the methodology discussed in the main paper. All geometries presented here were obtained with counterpoise corrections for BSSE using the def2-TZVPP basis set (very similar to the CP2K TZV2P basis set) in Gaussian 16. Two types of damping for the Grimme D3 dispersion corrections were utilized: Becke–Johnson damping

(damping dispersion to a parameterized constant at short interatomic distances, D3BJ) and "zero-damping" (damping to 0 at short interatomic distances, D3(0)).

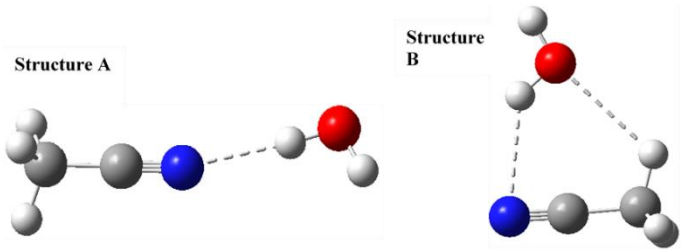

Figure 4.2 MP2 optimized structures of H_2O paired with acetonitrile.

Hydrogen bond lengths were measured between hydrogen and heavy atom and shown in Table 4.1. H---N for structure A, H---N and H---C for structure B, donor-hydrogen-acceptor angle reported in degrees. The BLYP-D3(0) minimum structure for B displays nearly equal lengths for both hydrogen bond contacts, whereas every other method favors a shorter N---H distance by ~0.15 to 0.3 Angstroms. Starting from multiple structures, BLYP-D3(0) converges to this structure and BLYP-D3BJ always converges to a shorter N---H bond length, even when both start from the other's optimized structure.

Table 4.1 Hydrogen bond distances (Å) and angles (º)

Method	A: $d_{(H---N)}$ // $\angle_{OHN}$	B: $d_{(H---N)}$ // $\angle_{OHN}$	A: $d_{(H---O)}$ // $\angle_{CHO}$
BLYP-D3(0)	2.08 // 176.4	2.57 // 135.2	2.58 // 123.4
BLYP-D3BJ	2.08 // 176.3	2.42 // 140.5	2.72 // 119.4
CAM-B3LYP-D3BJ	2.05 // 177.5	2.40 // 137.8	2.61 // 120.1

MP2	**2.10 // 176.5**	**2.43 // 137.6**	**2.68 // 119.5**

Table 4.2 Complexation energies (kcal/mol) for each structure and their difference.

Method	A	B	A – B
BLYP-D3(0)	−4.63	−4.91	0.28
BLYP-D3BJ	−4.69	−4.58	−0.11
CAM-B3LYP-D3BJ	−5.22	−5.17	−0.05
MP2	−4.46	−4.42	−0.04
CCSD(T)//MP2	**−4.29**	**−4.24**	**−0.05**

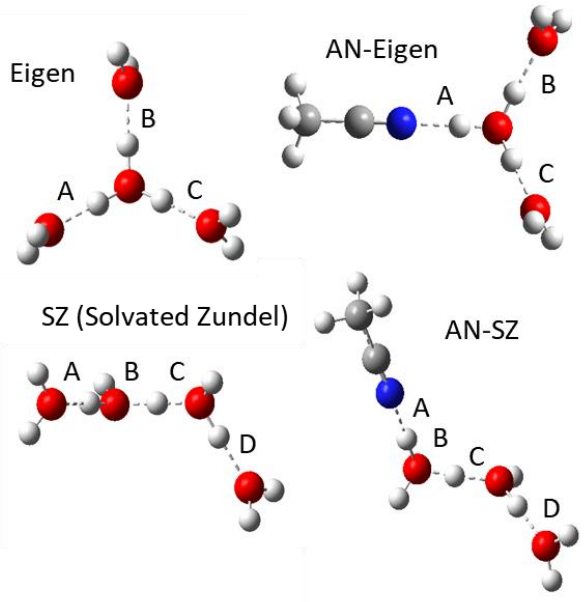

Figure 4.3 Structures selected for QTAIM analysis with labeled HBs.

The energy of the two complexes were calculated and shown in Table 4.2 (reported in kcal/mol, A – B difference reported in 3rd column, calculated using the counterpoise corrections and the supramolecular approach). CCSD(T) complexation energies obtained with MP2 geometries, as described in the text. The BLYP-D3(0) energy difference is abnormal; all other methods slightly favor structure A over structure B. Without counterpoise corrections (not reported), this trend is less uniform; however, BLYP-D3(0) still predicts a much larger (2-3 times) energy difference between the two structures. These abnormal results point to BLYP-D3BJ as a better match to higher levels of theory than BLYP-D3(0), and thus better suited for dynamics calculations.

4.3.2.2 Results of QTAIM on Protonated Water Clusters

In order to evaluate HB strengths, four representative structures were selected from the production run trajectories and optimized for subsequent QTAIM analysis. The purpose of the electronic structure and QTAIM analyses were two-fold: to characterize the two possible major $H_7O_3^+$ clusters with an associated acetonitrile, and to benchmark the DFT method (BLYP-D3(0) or BLYP-D3BJ) results used in AIMD against higher levels of theory. In particular, we considered the results of the CCSD(T) method (obtained from single-point energy calculations on the MP2 optimized geometries, referred to as CCSD(T)//MP2) and the range-separated hybrid functional CAM-B3LYP-D3BJ as references.

The selected structures are depicted in Figure 4.3. The fully water clusters shown in Figure 4.3 are either Eigen or “solvated Zundel” cations. The “AN” clusters are analogous to the water clusters with one molecule replaced by an acetonitrile to form acetonitrile + $H_7O_3^+$ cations. Table 4.3 provides the zero-point corrected energy differences between the Eigen and Zundel protonated

water clusters, as well as the differences between the equivalent AN clusters. For all examined levels of theory, the Eigen cluster was found to be lower in energy than that of the solvated Zundel for both water and AN clusters. However, CCSD(T) results suggest that the inclusion of acetonitrile increases the favorability of the Eigen over that of the solvated Zundel topology by 1 kcal/mol. This difference decreases slightly from CCSD(T) to CAM-B3LYP-D3BJ to BLYP-D3BJ. Meanwhile, the BLYP-D3(0) results display an opposite trend, whereby the energy difference is expected to decrease with an associated acetonitrile. This deviation from the higher levels of theory likely arises from short-term repulsive effects associated with the decrease of the dispersion term to zero at short distances, which could potentially play a role in AIMD trajectories.[24] Due to its closer adherence to higher levels of theory, BLYP-D3BJ was used for all analysis going forward over BLYP-D3(0).

Table 4.3 Energy differences between clusters, obtained as described in methods.

ΔE (kcal/mol)	CCSD(T)//MP2	CAM-B3LYP-D3BJ	BLYP-D3BJ	BLYP-D3(0)
ΔW: SZ – E	2.50	2.01	1.69	2.33
ΔAN: AN-SZ – AN-E	3.56	2.79	2.25	1.75
ΔAN – ΔW:	**1.06**	**0.78**	**0.56**	**–0.58**

Table 4.4 lists the BLYP-D3BJ HB parameters for each cluster shown in Figure 4.3. In considering the HB bond lengths, there is minimal difference between the Eigen water cluster and AN-Eigen, with the HB associated with acetonitrile only slightly decreasing in length. This analysis also bears out when considering the potential energy density obtained at the bcp, which

is a more robust indicator of hydrogen bond strength than length.[44, 46] Clearly, "AN-Eigen" is an Eigen cation with one water replaced by acetonitrile that only slightly perturbs the overall charge distribution, length, and hydrogen bond strength. The acetonitrile molecule in an AN-Eigen structure behaves like a water molecule (this is further discussed in Section 4.3.4), making the $H_7O_3^+$ cluster more of a AN-substituted Eigen cation as opposed to a Zundel cation.

Table 4.4 BLYP-D3BJ HB bond lengths (Å, hydrogen to acceptor distance) and bcp potential energy density (a.u) for each structure. Values involving the solvated proton in the Zundel clusters are bolded.

Structure	**Hydrogen Bond**			
	A	**B**	**C**	**D**
Eigen	1.55//−0.069	1.55//−0.069	1.55//−0.069	
AN-Eigen	1.58//−0.064	1.57//−0.067	1.57//−0.065	
SZ	1.57//−0.064	**1.21//−0.263**	**1.22//−0.248**	1.55//−0.061
AN-SZ	1.55//−0.069	**1.12//−0.407**	**1.32//−0.156**	1.64//−0.051

Comparing hydrogen bonds B and C in structures SZ and AN-SZ suggests that the acetonitrile at the edge of a Zundel-like $H_7O_3^+$ cluster induces a noticeable structural change, shifting the excess charge towards the edge. This localization of excess charge towards the edges was not observed in the free energy profiles described in Section 4.3.1; we attribute this observation to the fact that in a bulk acetonitrile solvation environment, acetonitrile molecules can coordinate the $H_7O_3^+$ cluster from both sides and balance the competition of the excess charge. However, the preferred energetics of the AN-Eigen cluster over the AN-SZ is unlikely to change

with increased solvation, making the identity of the experimentally observed $H_7O_3^+$ cluster most probably AN-Eigen as opposed to AN-SZ.

4.3.3 Measurements of Charge Delocalization

To further explicate the nature of the excess proton defect in protonated water clusters in acetonitrile, we developed two measurements for evaluating the magnitude of excess charge delocalization: δ and D_{O^*O}. δ is calculated as:

$$\delta = \left| d_{O^*H} - d_{O_WH} \right| \tag{4.2}$$

in which d_{O^*H} is the distance between the shared hydrogen atom and the hydronium oxygen, and d_{O_WH} is the distance between the shared hydrogen atom and the water oxygen atom. Note that both the shared hydrogen atom and the water oxygen belong to the special pair of the hydronium. A smaller δ (close to 0.0) indicates that the charge is shared between two water molecules and the hydrated excess proton is more geometrically Zundel-like. For this study, the SP was identified as the water molecule in the first solvation shell with the smallest δ value. Additionally, D_{O^*O} is defined as the distance between the hydronium oxygen atom and the SP oxygen atom. Our potential of mean force (PMF) calculations for both measurements are presented in Figure 4.4.

As indicated in Figure 4.4(a), the global minimum of δ PMF is located at $\delta = 0.34$, indicating that the excess proton is mostly localized in the acetonitrile-acid-water system and, overall, is Eigen-like. The global minimum of D_{O^*O} PMF located at $D_{O^*O} = 2.47\text{Å}$ is consistent with the findings of Elsaesser et al.,[7] who reported the shortest O···O distance of $H_9O_4^+$. This

outcome further validates our conclusion (see Section 4.3.1) that the predominant solvation species in acetonitrile is an $H_9O_4^+$ Eigen cation, rather than a Zundel cation.

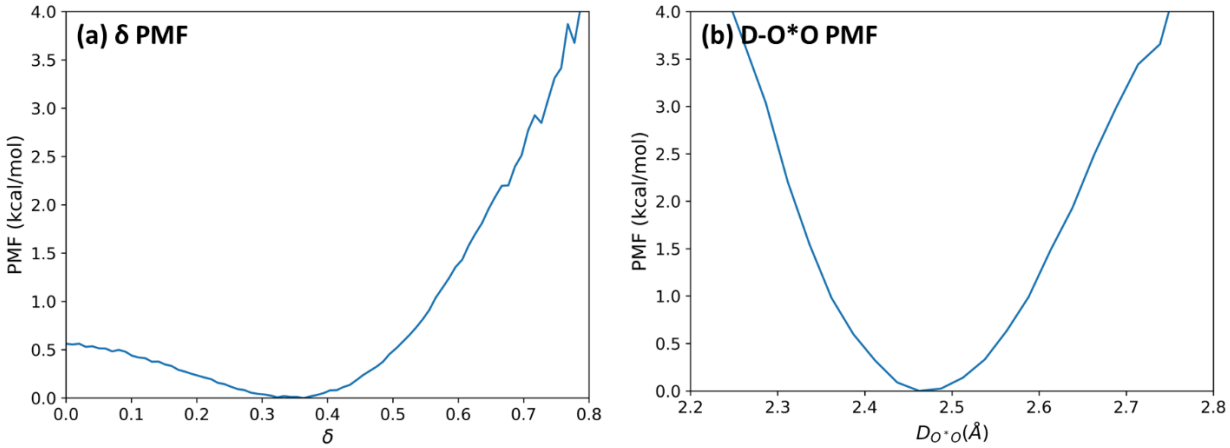

Figure 4.4 (a) PMF of $\boldsymbol{\delta}$, global minimum at 0.34; (b) PMF of $\boldsymbol{D_{O^*O}}$, global minimum at 2.47 Å

4.3.4 Structural Analysis of $H_7O_3^+$ and $H_9O_4^+$ Clusters

To better understand the structural properties of the two primary solvation species, $H_9O_4^+$ and $H_7O_3^+$, we calculated the O*-O (hydronium-water) distance distribution functions of $H_9O_4^+$ and $H_7O_3^+$ clusters using plain BLYP-D3BJ trajectories. The distance distribution function is defined as follows:

$$\rho_{O^*-O}(r) = \frac{1}{4\pi r^2}\langle \sum_{i \in O} \delta(|\boldsymbol{r_i} - \boldsymbol{r_{O^*}}| - r)\rangle \tag{4.3}$$

The distance distribution function is similar to the radial distribution function (RDF) but not normalized by the average density of the distribution species and should be preferred over RDF due to inhomogeneous environments in acetonitrile-acid-water systems. Accordingly, BLYP-D3BJ simulations were set up and equilibrated in the same manner as the aforementioned BLYP-

D3BJ umbrella-sampling simulations, but with two notable differences. First, the simulation boxes contained the 95 acetonitrile molecules, 1 iodine anion, and 1 protonated water cluster of interest ($H_9O_4^+$ / $H_7O_3^+$); second, no bias potential was applied. For both clusters, 50 ps of production trajectories were acquired. No conformation change was observed during the simulation and the clusters remained intact.

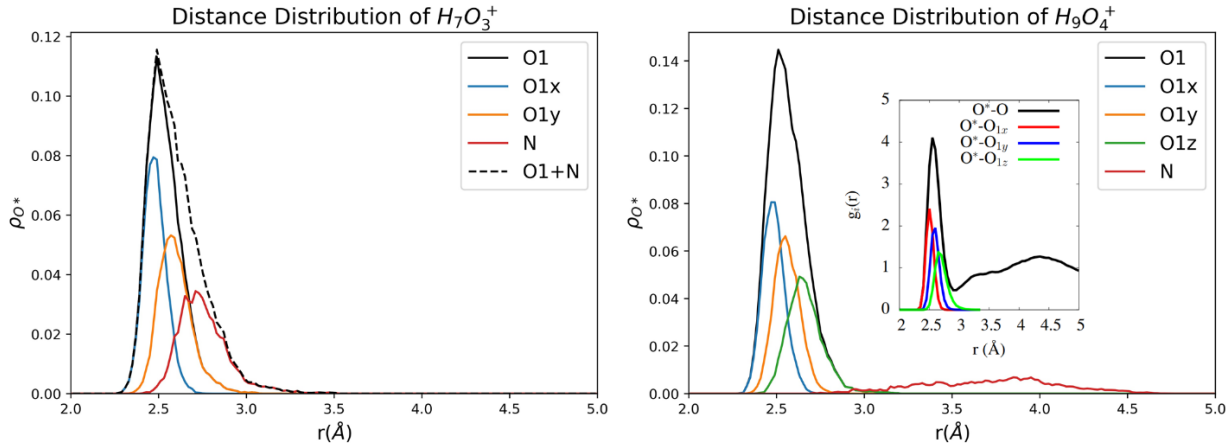

Figure 4.5 Overall and decomposed O*-O distance distribution functions of $H_7O_3^+$ and $H_9O_4^+$. The inset figure in the right panel presents overall and decomposed O*-O RDF in bulk water from a recent preprint.[51]

Figure 4.5 provides the overall and decomposed O*-O distance distribution functions of $H_7O_3^+$ and $H_9O_4^+$. The solid black line O1 denotes the total distributions. O1x, O1y and O1z are the closest (i.e., the SP), second closest and third closest oxygen atoms to the hydronium oxygen, respectively. The red line N denotes the distribution of the N atom from the closest acetonitrile molecule to O*. In the plot for $H_7O_3^+$ (Fig 4.5, left), the black dashed line O1+N denotes the summed distribution of the two O atoms and the closest N atom. In both clusters, the total O1 distributions can be decomposed into separate and distinct sub-distributions, indicating the

structural impact on protonated water clusters introduced by the presence of the SP. Furthermore, since the O1+N distribution and the O1x-O1y-N sub-distributions in $H_7O_3^+$ are similar to the O1 and O1x-O1y-O1z distributions in $H_9O_4^+$, we can conclude that for the $H_7O_3^+$ clusters, the closest acetonitrile molecule plays a role similar to O1z for the $H_9O_4^+$ clusters. This observation further validates our conclusions presented in Section 4.3.2 that the $H_7O_3^+$ cluster is an AN-substituted distorted Eigen cation, rather than a Zundel cation with one extra water molecule.

Elsaesser et al.[16] stated that the Eigen/Zundel cutoff of D_{O^*O} should be set at 2.7 Å. They also pointed out that species with a D_{O^*O} smaller than 2.7 Å should be classified as Zundel-type. However, based on our recent findings,[51] this cutoff is in general too aggressive. The inset figure in the right panel of Figure 4.5 shows total and decomposed RDFs of O*-O in bulk water, calculated from trajectories obtained via Experiment Directed Simulation[52]for *Ab Initio* Molecular Dynamics(EDS-AIMD).[53] The RDFs for the bulk system and the distance distribution functions of $H_9O_4^+$ are similar, indicating that the $H_9O_4^+$ cluster in acetonitrile resembles an Eigen cation in bulk water and preserves the bulk structural properties. However, if we apply a cutoff of 2.7 Å, under almost no circumstance can an Eigen cation be identified, either in bulk water or in protonated water clusters in acetonitrile.

4.3.5 Special Pair Lifetimes and Anisotropy

We calculated the continuous correlation function for the special pair (O1x) in $H_7O_3^+$ and $H_9O_4^+$ in acetonitrile using the BLYP-D3BJ trajectories introduced above and the following equation:

$$C_1(t) = \frac{\langle h(0)h(t)\rangle}{\langle h(0)\rangle} \tag{4.4}$$

where $h(t) = 1$ for continuous segments in the trajectory where the identity of O1x remains the same and $h(t) = 0$ otherwise; the bra-kets denote both an ensemble average and a time average. The plots of $C_1(t)$ are presented in Figure 4.6(a). By integrating the continuous correlation functions, we calculated the SP lifetimes in $H_7O_3^+$ and $H_9O_4^+$ to be 39.0 fs and 16.1 fs, respectively. Note that the SP lifetime for $H_9O_4^+$ was found to be comparable to that of excess proton in bulk water (15.7 fs).[51] When considered in tandem with our structural analysis results (Section 4.3.4), we conclude that the primary protonated water cluster species in acetonitrile, $H_9O_4^+$, preserves both structural and dynamical properties of the distorted Eigen cations in bulk water. The SP lifetime for $H_7O_3^+$ in acetonitrile was found to be noticeably longer than that of $H_9O_4^+$ and bulk Eigen cation. This finding is not surprising as there is one less water molecule in the cluster for SP presence. If the $H_7O_3^+$ were truly a Zundel cation, observation of a shorter SP lifetime would be expected, since the excess proton would be rattling between two water molecules rapidly, exchanging the identity of hydronium and SP.

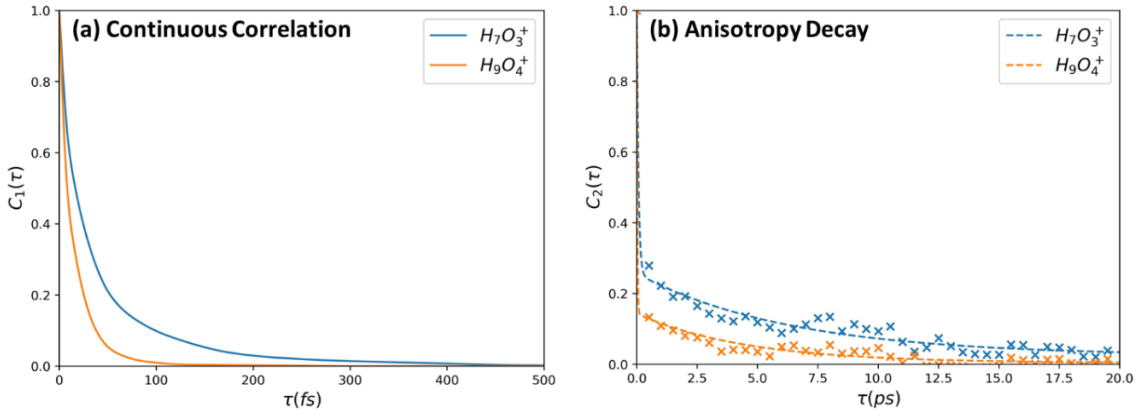

Figure 4.6 (a) Continuous correlation function $\boldsymbol{C_1(t)}$ of $H_7O_3^+$ and $H_9O_4^+$ in acetonitrile. (b) Anisotropy decay function $\boldsymbol{C_2(t)}$ of $H_7O_3^+$ and $H_9O_4^+$

We next investigated the anisotropy of the special pairs in these water clusters. The anisotropy calculation was defined with the following equation:

$$C_2(t) = \frac{\langle P_2(\hat{u}(t)\hat{u}(0))\rangle}{\langle P_2(\hat{u}(0)\hat{u}(0))\rangle} \tag{4.5}$$

in which $\hat{u}$ is the unit vector along O*-O axis of the special pair, and P_2 denotes the second Legendre polynomial. Anisotropy decays, calculated for both acetonitrile $H_7O_3^+$ and $H_9O_4^+$, are shown in Figure 4.6(b). In one of our recent studies on the excess proton in bulk water, we established that anisotropy decay is a combination of three processes: 1) the special pair dance, 2) the diffusive rotation of the protonated water cluster, and 3) the contribution of proton transport.[51] However, given the absence of proton transport in the isolated water clusters, bi-exponential fit ($a_1 \exp(-t/\tau_1) + a_2 \exp\left(-\frac{t}{\tau_2}\right) + C$) was applied to account for the first two processes. The fit results are shown in Table 4.5. The shorter timescale of tens of femtoseconds corresponds to the special pair dance. The SP dance timescale for the protonated water cluster $H_9O_4^+$ was found to be comparable to that of bulk. Conversely, the analogous data for $H_7O_3^+$ was noted to be much longer, which is consistent with the aforementioned SP lifetime results. The longer process corresponds to the diffusive rotation of the protonated water clusters, which tends to be significantly slower in clusters in acetonitrile than in bulk water. This difference can be understood in terms of the strong polarity of acetonitrile molecules, as well as by considering the strong interaction of acetonitrile molecules to the water clusters (see Section 4.3.2). We also point out that the diffusive rotation process of an $H_7O_3^+$ cluster is noticeably slower in comparison to $H_9O_4^+$, which can be explained by the fact that $H_7O_3^+$ is a distorted Eigen cation with one water substituted by an acetonitrile molecule (as shown in Figure 4.5 right panel). The diffusive rotation process of $H_7O_3^+$ is hampered by the heavier acetonitrile molecule closely associated in the cluster structure.

Table 4.5 Bi-exponential fit results of SP anisotropy decay in $H_7O_3^+$, $H_9O_4^+$ and bulk water.

Species	a_1	τ_1 (fs)	a_2	τ_2 (ps)	C
$H_7O_3^+$	0.77	67	0.23	6.39	0.02
$H_9O_4^+$	0.86	20	0.14	4.51	0.004
Bulk[51]	0.68	28	0.32	0.29	0.06

4.4 Conclusions

This study incorporated DFT-based AIMD, QTAIM, and MS-EVB methodologies to investigate the thermodynamics, structural, and dynamical properties of protonated water clusters solvated in acetonitrile. Based on data from AIMD umbrella sampling simulations, we identified $H_9O_4^+$ and $H_7O_3^+$ as the first- and second-most dominant species of protonated water clusters in acetonitrile. Using structural and dynamical analysis results obtained from plain AIMD trajectories, we found that the primary solvation species in acetonitrile, $H_9O_4^+$, resembles the distorted Eigen cations in bulk water with respect to their consistent structural and dynamical properties. Additionally, the QTAIM data analysis (Section 4.3.2), the distance distribution function (Section 4.3.4) and anisotropy decay (Section 4.3.5) results combined establish that the secondary solvation species, $H_7O_3^+$, is an acetonitrile-substituted distorted Eigen cation. The PMFs for charge delocalization measurements, presented in Section 4.3.3, also confirm that in these protonated water clusters in acetonitrile the excess charge is localized and Eigen-like. The heavier and more polar acetonitrile molecules interact strongly with the water molecules and slow down the diffusive movements of the clusters. The findings from this investigation demonstrate that even

with stoichiometric control, an acetonitrile-acid-water system is more complex than a "Zundel cation solution" and can contain a multitude of species with predominant Eigen-like protonated water clusters.

4.5 References

1. Tuckerman, M.; Laasonen, K.; Sprik, M.; Parrinello, M., Ab Initio Molecular Dynamics Simulation of the Solvation and Transport of H3o+ and Oh-Ions in Water. *The Journal of Physical Chemistry* **1995**, *99*, 5749-5752.

2. Tuckerman, M.; Laasonen, K.; Sprik, M.; Parrinello, M., Ab Initio Molecular Dynamics Simulation of the Solvation and Transport of Hydronium and Hydroxyl Ions in Water. *The Journal of chemical physics* **1995**, *103*, 150-161.

3. Schmitt, U. W.; Voth, G. A., The Computer Simulation of Proton Transport in Water. *The Journal of chemical physics* **1999**, *111*, 9361-9381.

4. Markovitch, O.; Chen, H.; Izvekov, S.; Paesani, F.; Voth, G. A.; Agmon, N., Special Pair Dance and Partner Selection: Elementary Steps in Proton Transport in Liquid Water. *The Journal of Physical Chemistry B* **2008**, *112*, 9456-9466.

5. Swanson, J. M.; Simons, J., Role of Charge Transfer in the Structure and Dynamics of the Hydrated Proton. *The Journal of Physical Chemistry B* **2009**, *113*, 5149-5161.

6. Thämer, M.; De Marco, L.; Ramasesha, K.; Mandal, A.; Tokmakoff, A., Ultrafast 2d Ir Spectroscopy of the Excess Proton in Liquid Water. *Science* **2015**, *350*, 78-82.

7. Kundu, A.; Dahms, F.; Fingerhut, B. P.; Nibbering, E. T.; Pines, E.; Elsaesser, T., Hydrated Excess Protons in Acetonitrile/Water Mixtures: Solvation Species and Ultrafast Proton Motions. *The journal of physical chemistry letters* **2019**, *10*, 2287-2294.

8. Dahms, F.; Fingerhut, B. P.; Nibbering, E. T.; Pines, E.; Elsaesser, T., Large-Amplitude Transfer Motion of Hydrated Excess Protons Mapped by Ultrafast 2d Ir Spectroscopy. *Science* **2017**, *357*, 491-495.

9. Fournier, J. A.; Carpenter, W. B.; Lewis, N. H.; Tokmakoff, A., Broadband 2d Ir Spectroscopy Reveals Dominant Asymmetric H 5 O 2+ Proton Hydration Structures in Acid Solutions. *Nature chemistry* **2018**, *10*, 932-937.

10. Carpenter, W. B.; Fournier, J. A.; Lewis, N. H.; Tokmakoff, A., Picosecond Proton Transfer Kinetics in Water Revealed with Ultrafast Ir Spectroscopy. *The Journal of Physical Chemistry B* **2018**, *122*, 2792-2802.

11. Carpenter, W. B.; Lewis, N. H.; Fournier, J. A.; Tokmakoff, A., Entropic Barriers in the Kinetics of Aqueous Proton Transfer. *The Journal of chemical physics* **2019**, *151*, 034501.

12. Partington, J.; Cowley, E., Dipole Moment of Acetonitrile. *Nature* **1935**, *135*, 474-474.

13. Schmitt, U. W.; Voth, G. A., Multistate Empirical Valence Bond Model for Proton Transport in Water. *The Journal of Physical Chemistry B* **1998**, *102*, 5547-5551.

14. Day, T. J.; Soudackov, A. V.; Čuma, M.; Schmitt, U. W.; Voth, G. A., A Second Generation Multistate Empirical Valence Bond Model for Proton Transport in Aqueous Systems. *The Journal of chemical physics* **2002**, *117*, 5839-5849.

15. Wu, Y.; Chen, H.; Wang, F.; Paesani, F.; Voth, G. A., An Improved Multistate Empirical Valence Bond Model for Aqueous Proton Solvation and Transport. *The Journal of Physical Chemistry B* **2008**, *112*, 467-482.

16. Park, K.; Lin, W.; Paesani, F., A Refined Ms-Evb Model for Proton Transport in Aqueous Environments. *The Journal of Physical Chemistry B* **2012**, *116*, 343-352.

17. Biswas, R.; Tse, Y.-L. S.; Tokmakoff, A.; Voth, G. A., Role of Presolvation and Anharmonicity in Aqueous Phase Hydrated Proton Solvation and Transport. *The Journal of Physical Chemistry B* **2016**, *120*, 1793-1804.

18. Martínez, L.; Andrade, R.; Birgin, E. G.; Martínez, J. M., Packmol: A Package for Building Initial Configurations for Molecular Dynamics Simulations. *Journal of computational chemistry* **2009**, *30*, 2157-2164.

19. Plimpton, S., Fast Parallel Algorithms for Short-Range Molecular Dynamics. *Journal of computational physics* **1995**, *117*, 1-19.

20. Becke, A., Phys. Rev. A: At., Mol., Opt. Phys. **1988**.

21. Lee, C.; Yang, W.; Parr, R., Phys. Rev. B: Condens. Matter Mater. Phys. **1988**.

22. Goedecker, S.; Teter, M.; Hutter, J., Separable Dual-Space Gaussian Pseudopotentials. *Physical Review B* **1996**, *54*, 1703.

23. Ehrlich, S.; Moellmann, J.; Reckien, W.; Bredow, T.; Grimme, S., System-Dependent Dispersion Coefficients for the Dft-D3 Treatment of Adsorption Processes on Ionic Surfaces. *ChemPhysChem* **2011**, *12*, 3414-3420.

24. Grimme, S.; Ehrlich, S.; Goerigk, L., Effect of the Damping Function in Dispersion Corrected Density Functional Theory. *Journal of computational chemistry* **2011**, *32*, 1456-1465.

25. VandeVondele, J.; Krack, M.; Mohamed, F.; Parrinello, M.; Chassaing, T.; Hutter, J., Quickstep: Fast and Accurate Density Functional Calculations Using a Mixed Gaussian and Plane Waves Approach. *Computer Physics Communications* **2005**, *167*, 103-128.

26. Tribello, G. A.; Bonomi, M.; Branduardi, D.; Camilloni, C.; Bussi, G., Plumed 2: New Feathers for an Old Bird. *Computer Physics Communications* **2014**, *185*, 604-613.

27. Bonomi, M.; Branduardi, D.; Bussi, G.; Camilloni, C.; Provasi, D.; Raiteri, P.; Donadio, D.; Marinelli, F.; Pietrucci, F.; Broglia, R. A., Plumed: A Portable Plugin for Free-Energy Calculations with Molecular Dynamics. *Computer Physics Communications* **2009**, *180*, 1961-1972.

28. Becke, A. D., Density-Functional Exchange-Energy Approximation with Correct Asymptotic Behavior. *Physical Review A* **1988**, *38*, 3098-3100.

29. Lee, C.; Yang, W.; Parr, R. G., Development of the Colle-Salvetti Correlation-Energy Formula into a Functional of the Electron Density. *Physical Review B* **1988**, *37*, 785-789.

30. Miehlich, B.; Savin, A.; Stoll, H.; Preuss, H., Results Obtained with the Correlation Energy Density Functionals of Becke and Lee, Yang and Parr. *Chemical Physics Letters* **1989**, *157*, 200-206.

31. Grimme, S.; Antony, J.; Ehrlich, S.; Krieg, H., A Consistent and Accurate Ab Initio Parametrization of Density Functional Dispersion Correction (Dft-D) for the 94 Elements H-Pu. *The Journal of Chemical Physics* **2010**, *132*, 154104.

32. Weigend, F.; Ahlrichs, R., Balanced Basis Sets of Split Valence, Triple Zeta Valence and Quadruple Zeta Valence Quality for H to Rn: Design and Assessment of Accuracy. *Physical Chemistry Chemical Physics* **2005**, *7*, 3297-3305.

33. Vosko, S. H.; Wilk, L.; Nusair, M., Accurate Spin-Dependent Electron Liquid Correlation Energies for Local Spin Density Calculations: A Critical Analysis. *Canadian Journal of Physics* **1980**, *58*, 1200-1211.

34. Becke, A. D., Density-Functional Thermochemistry. Iii. The Role of Exact Exchange. *The Journal of Chemical Physics* **1993**, *98*, 5648-5652.

35. Stephens, P. J.; Devlin, F. J.; Chabalowski, C. F.; Frisch, M. J., Ab Initio Calculation of Vibrational Absorption and Circular Dichroism Spectra Using Density Functional Force Fields. *The Journal of Physical Chemistry* **1994**, *98*, 11623-11627.

36. Yanai, T.; Tew, D. P.; Handy, N. C., A New Hybrid Exchange–Correlation Functional Using the Coulomb-Attenuating Method (Cam-B3lyp). *Chemical Physics Letters* **2004**, *393*, 51-57.

37. Goerigk, L.; Grimme, S., A Thorough Benchmark of Density Functional Methods for General Main Group Thermochemistry, Kinetics, and Noncovalent Interactions. *Physical Chemistry Chemical Physics* **2011**, *13*, 6670-6688.

38. Head-Gordon, M.; Pople, J. A.; Frisch, M. J., Mp2 Energy Evaluation by Direct Methods. *Chemical Physics Letters* **1988**, *153*, 503-506.

39. Frisch, M. J.; Head-Gordon, M.; Pople, J. A., A Direct Mp2 Gradient Method. *Chemical Physics Letters* **1990**, *166*, 275-280.

40. Purvis, G. D.; Bartlett, R. J., A Full Coupled-Cluster Singles and Doubles Model: The Inclusion of Disconnected Triples. *The Journal of Chemical Physics* **1982**, *76*, 1910-1918.

41. Scuseria, G. E.; Janssen, C. L.; Schaefer, H. F., An Efficient Reformulation of the Closed-Shell Coupled Cluster Single and Double Excitation (Ccsd) Equations. *The Journal of Chemical Physics* **1988**, *89*, 7382-7387.

42. Pople, J. A.; Head-Gordon, M.; Raghavachari, K., Quadratic Configuration Interaction. A General Technique for Determining Electron Correlation Energies. *The Journal of Chemical Physics* **1987**, *87*, 5968-5975.

43. Lu, T.; Chen, F., Multiwfn: A Multifunctional Wavefunction Analyzer. *J. Comput. Chem.* **2012**, *33*, 580-592.

44. Beckett, D.; El-Baba, T. J.; Gilbert, K.; Clemmer, D. E.; Raghavachari, K., Untangling Hydrogen Bond Networks with Ion Mobility Spectrometry and Quantum Chemical Calculations: A Case Study on H+Xpgg. *J. Phys. Chem. B* **2019**, *123*, 5730-5741.

45. Koch, U.; Popelier, P. L. A., Characterization of C-H-O Hydrogen Bonds on the Basis of the Charge Density. *J. Phys. Chem.* **1995**, *99*, 9747-9754.

46. Espinosa, E.; Molins, E.; Lecomte, C., Hydrogen Bond Strengths Revealed by Topological Analyses of Experimentally Observed Electron Densities. *Chemical Physics Letters* **1998**, *285*, 170-173.

47. Knight, C.; Lindberg, G. E.; Voth, G. A., Multiscale Reactive Molecular Dynamics. *Journal of Chemical Physics* **2012**, *137*, 22A525.

48. Schmitt, U. W.; Voth, G. A., The Computer Simulation of Proton Transport in Water. *Journal of Chemical Physics* **1999**, *111*, 9361-9381.

49. Yamashita, T.; Peng, Y.; Knight, C.; Voth, G. A., Computationally Efficient Multiconfigurational Reactive Molecular Dynamics. *Journal of chemical theory and computation* **2012**, *8*, 4863-4875.

50. Peng, Y.; Knight, C.; Blood, P.; Crosby, L.; Voth, G. A. In *Extending Parallel Scalability of Lammps and Multiscale Reactive Molecular Simulations*, Proceedings of the 1st Conference of

the Extreme Science and Engineering Discovery Environment: Bridging from the eXtreme to the Campus and Beyond, 2012; pp 1-7.

51. Calio, P. B.; Li, C.; Voth, G. A., Understanding the Essential Nature of the Hydrated Excess Proton through Simulation and Interpretation of Recent Spectroscopic Experiments. *arXiv preprint arXiv:2101.01782* **2021**.

52. White, A. D.; Voth, G. A., Efficient and Minimal Method to Bias Molecular Simulations with Experimental Data. *Journal of chemical theory and computation* **2014**, *10*, 3023-3030.

53. White, A. D.; Knight, C.; Hocky, G. M.; Voth, G. A., Improved Ab Initio Molecular Dynamics by Minimal Biasing with Experimental Data. *arXiv preprint arXiv:1607.00251* **2016**.

CHAPTER 5

CONCLUDING REMARKS

A series of work have been done in the effort to understand the behaviors of hydrated excess proton in complex aqueous systems.

In CHAPTER 2, we employed both the MS-EVB method and DFT-based AIMD to investigate the interfacial behavior of a hydrated excess proton with respect to two different definitions of interfaces. As detailed herein, the GDI and WCI afforded similar results demonstrating that the excess proton tends to reside at the interface for either CV; moreover, our EVB 3.2 and AIMD results are broadly consistent with one another. A composite 2D PMF constructed from the two CV definitions of interface showed a high degree of good correlation between the results of two CVs, with that correlation somewhat weakening when the excess proton moves near and past the interface. We attribute this weakened correlation beyond the interface to the charged water cluster formed around the excess proton that interrupts the interfacial density field, which in turn influences the location and shape of the WCI. Due to its dependence on the coordinates of the CEC of the hydrated excess proton, the WCI has difficulty disentangling the interfacial thermodynamics of the excess proton from the influence on the surface curvaturs induced by the excess proton itself. This work reaffirms the likelihood that the hydrated excess proton has an affinity for the air-water interface no matter how that interface is defined – a result that is consistent with the original prediction made in sixteen years ago and now supported by a significant body of experimental results, include two very recent studies.

In CHAPTER 3, we performed MS-RMD simulations of one hydrated excess proton in non-ionic reverse micelles of four varying sizes, with the goal of determining the general impact on the behavior of the excess proton posed by the confinement in these micelles. Our simulations

present a microscopic analysis of micellar water pool behavior consistent with prior research efforts. In our reverse micelles, the hydrated excess proton remains near the interface and interacts with surfactant head groups, which participates in the formation of a second solvation shell. The hydrated excess proton is found to be localized both radially and laterally near the interface. This investigation also confirmed that proton transport is slow in reverse micelles, which we ascribe to both the slow vehicular motion of hydronium-like cations and a lower proton Grotthuss hopping rate. The former tendency is also connected to the slow diffusion of interfacial water, which is consistent with previous theoretical and experimental findings. To further elucidate the impact of the low proton hopping rate, we analyzed the structure of the hydronium-like complex. The resulting data confirmed that slow proton hopping occurs as a result of both the enhanced interfacial solvation of the excess hydrated proton and the immobilization of the interfacial water. Low water density in the interfacial region (i.e., where the hydrated excess proton resides) makes it difficult for an excess proton to form a complete HB network around it, thus hindering the proton hopping. Moreover, the orientation of the hydronium is locked because of the difficulty in rearranging the existing HB network and forming a new one. For the overall HB network, we observed a bi-exponential decay of the micellar HB autocorrelation function involving (a) short-range HB relaxation, and (b) long-range micellar solvation of HB pairs. The two relaxation times, τ_1 and τ_2, both showed a monotonic decreasing trend with increasing micellar size. In particular, we can attribute micellar water relaxation to the short-range τ_1, and micellar HB pair diffusion to the long-range τ_2. With increasing micellar size, the hydrated excess proton more easily leaves from the interface and the surrounding solvation environment becomes less interface-like and more bulk-like, thus decreasing the relaxation time for both processes.

In CHAPTER 4, we incorporated DFT-based AIMD, QTAIM, and MS-EVB methodologies to investigate the thermodynamics, structural, and dynamical properties of protonated water clusters solvated in acetonitrile. Based on data from AIMD umbrella sampling simulations, we identified $H_9O_4^+$ and $H_7O_3^+$ as the first- and second-most dominant species of protonated water clusters in acetonitrile. Using structural and dynamical analysis results obtained from plain AIMD trajectories, we found that the primary solvation species in acetonitrile, $H_9O_4^+$, resembles the distorted Eigen cations in bulk water with respect to their consistent structural and dynamical properties. Additionally, the QTAIM data analysis, the distance distribution function, and anisotropy decay results combined establish that the secondary solvation species, $H_7O_3^+$, is an acetonitrile-substituted distorted Eigen cation. The PMFs for charge delocalization measurements also confirm that in these protonated water clusters in acetonitrile the excess charge is localized and Eigen-like. The heavier and more polar acetonitrile molecules interact strongly with the water molecules and slow down the diffusive movements of the clusters. The findings from this investigation demonstrate that even with stoichiometric control, an acetonitrile-acid-water system is more complex than a "Zundel cation solution" and can contain a multitude of species with predominant Eigen-like protonated water clusters.

Throughout these projects, we observed some common behaviors of hydrated excess protons in heterogeneous, complex aqueous systems. The dynamics of the excess proton is stagnated near the hydrophobic phase (surfactant, vacuum or interface in general) – the proton hopping rate is decreased, the vehicular diffusion of the hydronium is slowed, the orientation of the hydronium is locked that the lone pair points towards the hydrophobic phase and rearrangement of the local hydrogen bond network is limited. These behaviors are a result of the amphiphilic property of the hydronium – the lone pair on the oxygen atom interacts with the hydrophobic phase,

thus hindering the excess proton from hopping away, which in turn slows the diffusion of the excess proton and limits the dynamics of HB network. Furthermore, we see that regardless of the solvation environment, certain features of the hydrated excess proton persist: the consistent structures of the hydronium and its first solvation shell and the special pair dance. We observe even in scattered small, protonated water clusters that the hydronium still performs the special pair dance when there are only one or two water molecules in its first solvation shell. The primary solvation motif remains an Eigen cation, even when there is no access to a complete solvation shell.

Looking forward, based on what I have investigated and discovered, one may embark on several directions to gain a better knowledge of the hydrated excess protons. One may further investigate the amphiphilic property of the hydronium cations, about the nature, the limit and the possible applications of such property, in a variety of systems like proton exchange membranes or biological systems. As we have established the primary solvation motif of the hydrated excess proton, one may also investigate the possible limit of this finding and see if there can be a carefully designed chemical environment where the primary solvation motif become a Zundel cation – In that case, one may acquire spectroscopic data of a Zundel cation solution as a reference and further our understanding of hydrated Zundel cations from an experimental point of view.